JFM PAPERS

An investigation of rotor aeroacoustics with unsteady motions and uncertainty factors

Siyang Zhong[1,†], **Peng Zhou**[2], **Wangqiao Chen**[2], **Hanbo Jiang**[3], **Han Wu**[2] and **Xin Zhang**[2,4]

[1]Department of Aeronautical and Aviation Engineering, The Hong Kong Polytechnic University, Hung Hom, Kowloon, Hong Kong SAR, PR China

[2]Department of Mechanical and Aerospace Engineering, The Hong Kong University of Science and Technology, Clear Water Bay, Kowloon, Hong Kong SAR, PR China

[3]Eastern Institute for Advanced Study, Yongriver Institute of Technology, Ningbo, PR China

[4]HKUST-Shenzhen Research Institute, Shenzhen 518057, PR China

The aeroacoustic characteristics of flying vehicles with pitch-fixed rotors differ from traditional helicopters with pitch-controlled rotor blades. Accurate predictions of rotor noise are still challenging because many uncertainty factors and unsteadinesses exist. This work investigates the aeroacoustic effects of rotational speed deviation, rotation speed fluctuation, blade vibration and blade geometric asymmetry. The analysis is based on the efficient computation of rotor noise under different working conditions. The mean aerodynamic variables are computed using the blade element moment theory, while small-amplitude fluctuations are introduced to account for the unsteadiness and uncertainty factors. It is shown that periodic rotation speed fluctuations and blade vibrations can produce significant extra tones. By contrast, if the fluctuations and vibrations are random, the noise level in a wide frequency range is increased. The intriguing result reminds us of the need to revisit the rotor broadband noise sources commonly attributed to turbulent flows. The influences are observer angle dependent, and the extra noise production is more significant in the upstream and downstream directions. The asymmetric blade geometry can cause extra tonal noise at the harmonics of the blade shaft frequency. The noise features of dual rotors are also investigated. Usually, the noise is sensitive to the initial phase difference and rotation directions due to the interference effect. However, the noise features are vastly altered if there are slight differences in the rotation speeds. Although the influences of some factors on rotor noise were already known, the present study provides a more comprehensive analysis of the problem. The results also

† Email address for correspondence: siyang.zhong@polyu.edu.hk

highlight the need to consider these practical factors for accurate noise prediction of multi-rotor flying vehicles.

Key words: aeroacoustics

1. Introduction

In the last decade, small-sized drones have been rapidly developed and widely employed in many civilian applications (Floreano & Wood 2015; Yao, Wang & Su 2016). With the tremendous success of the relevant industry and applications of drones, the development of urban air mobility vehicles with larger sizes and weights has attracted interest (Rajendran & Srinivas 2020; Donateo *et al.* 2021). However, one likely limiting factor of the development will be the annoying noise pollution during operations of the vehicles in urban regions (Al Haddad *et al.* 2020; Watkins *et al.* 2020). Multiple rotors are often used in these vehicles to provide the needed forces and to realise manoeuvred flights. Consequently, the rotor operations can generate significant aerodynamic noise containing tonal and broadband contents.

Many studies have been conducted to understand the mechanisms of rotor noise generation. A few pioneering and landmark studies linking noise emission with aerodynamic flow variables were performed by Gutin (1948), Deming (1937), Deming (1940), Arnoldi (1956), Lowson (1965), Lowson & Ollerhead (1969), Garrick & Watkins (1953) and Hubbard (1953), among others. A systematic approach to analysing the rotor noise is based on an acoustic analogy, which was initiated by Lighthill (1952) in unbounded flows and extended to problems with static boundaries by Curle (1955) and moving surfaces by Ffowcs Williams & Hawkings (1969) (FW-H). At low Mach numbers, the dominant noise sources are thickness noise and loading noise (Brentner & Farassat 1998). In the presence of background mean flows, Goldstein (1974) proposed an acoustic analogy with an inhomogeneous convected wave equation, which was the basis for the rotor noise prediction model by Hanson & Parzych (1993). The noise sources estimations were based on flow velocities and loadings on the blade surfaces, which can be obtained from computational fluid dynamics or computational aeroacoustics (CAA). Notably, near-field aerodynamic flows are resolved and employed as inputs of the surface integration to compute sound at given observers (Jiang & Zhang 2022). Usually, off-body integral solutions can suffer from spurious wave contamination if turbulent fluctuations pass through the integration surface (Wright & Morfey 2015), which was investigated in several recent studies (Shur, Spalart & Strelets 2005; Ikeda *et al.* 2013; Zhong & Zhang 2017, 2018).

However, rotor noise study is still challenging because the flow states are complex. Flow transitions can exist because of considerable differences in the Reynolds number from rotor tips to hubs. In addition, a tip vortex is formed on the pressure side of the rotor blade, rolled up to the suction side and eventually shed from the surface. The shedding frequency also depends on the total velocity and blade thickness (Kurtz & Marte 1970; Hubbard, Lansing & Runyan 1971). The tip vortex shedding can cause unsteady surface pressure and, therefore, significant noise generation (Preisser, Brooks & Martin 1994; Kim, Park & Moon 2019). The process is also influenced by the induced velocity of the vortex passing by the tip (George & Chou 1986; Preisser *et al.* 1994; Yung 2000). Moreover, in flight conditions, the vortex shed from a blade interacting with the adjacent blades can produce significant noise (Yung 2000) with varying directivity and strength (Splettstoesser *et al.* 1997). For small-sized drone rotors, experiments are essential, and various studies

have been conducted (Sinibaldi & Marino 2013; Zawodny, Boyd & Burley 2016; Ning, Wlezien & Hu 2017; Zhou & Fattah 2017; Fattah *et al.* 2019; Wu *et al.* 2020; Bu *et al.* 2021). However, there is an issue that the results are often laboratory dependent because the noise measurements are sensitive to various factors (Wu *et al.* 2022). For example, in confined chambers, the noise measurements can suffer from the flow recirculation effect (Stephenson, Weitsman & Zawodny 2019). There are other sources of uncertainty and unsteady factors due to the rotor motion and actual flying (Xu *et al.* 2020).

This study aims at understanding the influence of various unsteady and uncertain factors, which can present in practice, on rotor noise emission. The acoustic impact of some factors was partly known in the past, but a comprehensive analysis using a unified framework is still favoured. First, in practical applications, the torque ripples of electric motors (to drive the rotors) can cause rotation speed fluctuation (Islam *et al.* 2007), which was shown to significantly affect drone noise (Kim *et al.* 2021). The key reason is that the temporal variations of rotational speed can substantially increase the noise level (Wright 1971; Mani 1990) and alter noise spectra (Tinney & Sirohi 2018; McKay & Kingan 2019). Moreover, unsteadiness is inevitable in practical flying vehicles since the rotor speeds are adjusted by the real-time flight control (Davoudi *et al.* 2020; Djurek *et al.* 2020). Second, the rotor blades may experience oscillation (Marqués & Da Ronch 2017), which is common for helicopters with pitch control mechanisms and an aeroelastic effect (Leishman 2006). For fixed-pitch rotors for drones, vibration can exist due to the use of light and cost-effective materials. Notably, the flexibility of rotor blades can cause coupled oscillations (Biot 1940), which has been noticed for drone applications (Niemiec & Gandhi 2017; Nowicki 2017; Kuantama *et al.* 2021; Semke, Zahui & Schwalb 2021; Niemiec, Gandhi & Kopyt 2022). The effect of flow-induced vibrations is also an active research area for marine propellers (Tian *et al.* 2017). However, the corresponding aeroacoustic studies are rare. Last, the inevitable manufacturing tolerance, wear and looseness in practical applications can cause the long-standing problem of mass imbalance and aerodynamic asymmetry of rotor blades (Best 1945; Darlow 2012; Huo *et al.* 2020). The imbalance can result in structural vibration and extra noise generation (Altinors, Yol & Yaman 2021; Semke *et al.* 2021). For drones, many studies have been conducted to detect and control the rotor imbalance effect (Bondyra *et al.* 2017; de Jesus Rangel-Magdaleno *et al.* 2018; Ghalamchi, Jia & Mueller 2019; Iannace, Ciaburro & Trematerra 2019). Despite the (possibly) small amplitudes of these uncertainties and unsteadiness, the noise features will be significantly altered as sound contains only a tiny portion of the fluid energy.

It is difficult to quantify the effect of each factor experimentally because various mechanisms can coexist and be coupled in practice. Different factors can lead to similar impacts, making the exact causes indistinguishable. Capturing the instantaneous rotation speed variation and blade vibrations is also challenging for the instruments. Therefore, it is vital to understand the influence of each factor using more controllable approaches. In this view, high-fidelity numerical simulations could be helpful but are still too costly for parametric study. Therefore, theoretical analysis is still favoured to understand the key acoustic characteristics with various unsteady and uncertainty factors. The efficient computations using a unified framework will be helpful for more accurate and reliable noise assessment in complex working conditions.

For rotor noise prediction, Hanson & Parzych (1993) developed a frequency-domain model incorporating unsteady motions. Based on the model, Zhong *et al.* (2020) showed that periodic fluctuations can significantly increase the tonal noise levels at high frequencies. However, it only explained the behaviours of tones at harmonics of the blade passing frequency (BPF). For more generic applications, the unsteady motions might be transient and random, suggesting that noise computations based on time-domain

formulations will be more convenient. Like other aeroacoustic problems, rotor noise computation (Farassat 1981, 1986; Farassat & Brentner 1988; Farassat, Dunn & Spence 1992; Casalino 2003) can be based on the integral solution of the FW-H equation, especially the widely used Farassat formulation 1A (Farassat & Succi 1980). However, most of the studies were conducted for rotors with constant rotation speed, even though unsteady flows were considered (Gennaretti, Testa & Bernardini 2013). For unsteady manoeuvres, e.g. in the helicopter noise study by Gennaretti *et al.* (2015), a nonlinear equation was solved to estimate the time delay that is dependent on observer location, flight trajectory and blade kinematics. For rotors experiencing unsteady motion, evaluating the retarded time with the temporally varied source locations is difficult. This work will make efforts to ease the computations to facilitate the parametric studies.

In the following, § 2 introduces the rotor noise computation formulations with the unsteady motions and uncertainties considered. Section 3 presents verification and validation of the computation model, followed by the parametric study of rotation speed variation, blade vibration and asymmetry effects. Section 4 discusses the aeroacoustic influence on dual rotors, and § 5 is the summary.

2. Formulations for rotor noise computation

In this work, we start from the acoustic analogy by Goldstein (1974) to compute the rotor aerodynamic noise generation

$$\left(\frac{1}{a_\infty^2} \frac{\mathscr{D}^2}{\mathscr{D}t^2} - \nabla^2 \right) [p'H(f)] = \frac{\mathscr{D}}{\mathscr{D}t} \left[Q\delta(f) \right] - \frac{\partial}{\partial x_i} \left[L_i \delta(f) \right] + \frac{\partial^2}{\partial x_i \partial x_j} \left[T_{ij} H(f) \right], \quad (2.1)$$

where p' is sound pressure, a_∞ is speed of sound, $\boldsymbol{u}_\infty$ is the oncoming flow velocity and $\mathscr{D}/\mathscr{D}t = \partial/\partial t + \boldsymbol{u}_\infty \cdot \nabla$ is the material derivative. Also, $\delta(f)$ and $H(f)$ are the Dirac-δ function and Heaviside function with the argument of $f(\boldsymbol{x}(t)) = 0$ defining the blade surface geometry. The normal vector of the blade surface is $\boldsymbol{n} = \nabla f$, and the location $\boldsymbol{x}(t)$ satisfying $f(\boldsymbol{x}(t)) = 0$ varies in time due to the blade rotation. The tensor T_{ij} is represented as $T_{ij} = \rho u_i u_j + [(p - p_\infty) - c_\infty^2(\rho - \rho_\infty)]\delta_{ij} - \sigma_{ij}$, where ρ, p and u are the density, pressure and flow velocity. The subscript $(\cdot)_\infty$ means the variables in the uniform medium, δ_{ij} is the Kronecker-δ function and σ_{ij} is the viscosity tensor. Further, $\partial^2 T_{ij}/\partial x_i \partial x_j$ corresponds to the quadrupole noise source and can be omitted at low Mach numbers. Usually, u_i, p and σ_{ij} can be obtained by high-fidelity numerical simulations to evaluate L_i, corresponding to the aerodynamic loadings. However, for fast noise estimation, L_i can be approximated as the aerodynamic forces acting on the blade surfaces. Finally, $Q = [\rho(u_j + u_{\infty,j} - v_j) + \rho_\infty(v_j - u_{\infty,j})]n_j$ corresponds to the thickness noise, and v_j denotes velocity of the blade surface. At low Mach numbers, $\rho \approx \rho_\infty$ such that

$$Q \approx \rho_\infty u_j n_j. \quad (2.2)$$

2.1. *Solution for rotor noise with unsteady motions*

In this section, we introduce the solution to (2.1) for a rotor noise computation with the unsteady factors considered. Figure 1 illustrates the coordinates for both the observers $\boldsymbol{x} = (x_1, x_2, x_3)$ and source points $\boldsymbol{y} = (y_1, y_2, y_3)$. The two coordinate systems are aligned, $(\cdot)_1$ is in the axial direction, and $(\cdot)_2$ corresponds to the direction when the rotation phase angle $\phi = 0$. An observer described in the Cartesian system is related to the observer distance r_o, azimuthal angle φ and polar angle θ as

$$x_1 = r_o \cos \theta, \quad x_2 = r_o \sin \theta \cos \varphi, \quad x_3 = r_o \sin \theta \sin \varphi. \quad (2.3a\text{--}c)$$

The source point is linked to the radial location η and phase angle ϕ as

$$y_1 = y_1, \quad y_2 = \eta \cos \phi, \quad y_3 = \eta \sin \phi. \tag{2.4a–c}$$

Equation (2.1) can be solved by using the Green's function (Blokhintzev 1946; Najafi-Yazdi, Brès & Mongeau 2011)

$$G(\boldsymbol{x}, t; \boldsymbol{y}, \tau) = \frac{\delta(g)}{4\pi\mathscr{R}} = \frac{\delta(t - \tau - R/a_\infty)}{4\pi\mathscr{R}}, \quad \text{where } g = t - \tau - \frac{R}{a_\infty}, \tag{2.5}$$

where t and τ are the observer and source times. The two distances $\mathscr{R}$ and R are

$$\mathscr{R} = \beta\sqrt{r^2 + (\alpha\boldsymbol{M}_\infty \cdot \boldsymbol{r})^2}, \quad R = \alpha^2(\mathscr{R} - \boldsymbol{M}_\infty \cdot \boldsymbol{r}), \tag{2.6}$$

where $r = |\boldsymbol{r}| = |\boldsymbol{x} - \boldsymbol{y}|$, $\alpha = 1/\beta$, $\beta = \sqrt{1 - |\boldsymbol{M}_\infty|^2}$ and $\boldsymbol{M}_\infty = \boldsymbol{u}_\infty/a_\infty$. The spatial derivatives of $\mathscr{R}$ and $\mathcal{R}$ are computed

$$\tilde{\mathscr{R}}_i = \frac{\partial\mathscr{R}}{\partial x_i} = \frac{r_i + \alpha^2(\boldsymbol{M}_\infty \cdot \boldsymbol{r})M_{\infty,i}}{\alpha^2\mathscr{R}}, \quad \tilde{R}_i = \frac{\partial R}{\partial x_i} = \alpha^2(\tilde{\mathscr{R}}_i - M_{\infty,i}). \tag{2.7}$$

Then the sound pressure at the observer $\boldsymbol{x}$ and time t is computed as

$$p'(\boldsymbol{x}, t) = \frac{\partial}{\partial t} \int_{-\infty}^{t} \int_{\mathrm{R}^3} \frac{Q\delta(g)\delta(f)}{4\pi\mathscr{R}} \, \mathrm{d}\boldsymbol{y} \, \mathrm{d}\tau - \frac{\partial}{\partial x_i} \int_{-\infty}^{t} \int_{\mathrm{R}^3} \frac{(L_i - u_{\infty,i}Q)\delta(g)\delta(f)}{4\pi\mathscr{R}} \, \mathrm{d}\boldsymbol{y} \, \mathrm{d}\tau. \tag{2.8}$$

By using the property of the $\delta(f)$, each spatial integration in R^3 will be reduced to a surface integration on $f = 0$, i.e. (2.8) is written as

$$p'(\boldsymbol{x}, t) = \frac{\partial}{\partial t} \int_{-\infty}^{t} \int_{f=0} \frac{Q\delta(g)}{4\pi\mathscr{R}} \, \mathrm{d}S(\boldsymbol{y}) \, \mathrm{d}\tau - \frac{\partial}{\partial x_i} \int_{-\infty}^{t} \int_{f=0} \frac{(L_i - u_{\infty,i}Q)\delta(g)}{4\pi\mathscr{R}} \, \mathrm{d}S(\boldsymbol{y}) \, \mathrm{d}\tau. \tag{2.9}$$

In the second term, spatial derivatives $\partial/\partial x_i$ are applied to the computed integration term, which are undesired in practical applications. Fortunately, using the chain rule, we have (see also Brentner & Farassat 2003; Zhong & Zhang 2017)

$$\frac{\partial}{\partial x_i}\left(\frac{\delta(g)}{\mathscr{R}}\right) = -\frac{1}{a_\infty}\frac{\partial}{\partial t}\left(\frac{\tilde{R}_i\delta(g)}{\mathscr{R}}\right) - \frac{\tilde{\mathscr{R}}_i}{\mathscr{R}^2}\delta(g). \tag{2.10}$$

Therefore, the solution for $p'(\boldsymbol{x}, t)$ is written as

$$p'(\boldsymbol{x}, t) = \frac{\partial}{\partial t} \int_{-\infty}^{t} \int_{f=0} \left\{ \frac{Q + (L_i - u_{\infty,i}Q)\tilde{R}_i/a_\infty}{4\pi\mathscr{R}} \right\} \delta(g) \, \mathrm{d}S(\boldsymbol{y}) \, \mathrm{d}\tau$$

$$+ \int_{-\infty}^{t} \int_{f=0} \left\{ \frac{(L_i - u_{\infty,i}Q)\tilde{\mathscr{R}}_i}{4\pi\mathscr{R}^2} \right\} \delta(g) \, \mathrm{d}S(\boldsymbol{y}) \, \mathrm{d}\tau. \tag{2.11}$$

The argument of the δ-function $g = t - \tau - R/a_\infty$ is a smooth function of the source time τ. By using the composition rule of the Dirac-δ function, i.e. by making a change of
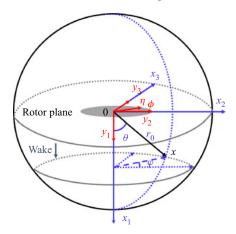
Figure 1. A schematic of the coordinate systems of the observer x and source points y.

variables from τ to g, the temporal integrations in (2.11) can be reduced to only evaluating values of the remaining terms when $g = 0$, i.e.

$$p'(x, t) = \frac{\partial}{\partial t} \int_{f=0} \left[\frac{Q + (L_i - u_{\infty,i}Q)\tilde{R}_i/a_\infty}{4\pi\mathcal{R}|\partial g/\partial\tau|} \right]_* \mathrm{d}S(y)$$
$$+ \int_{f=0} \left[\frac{(L_i - u_{\infty,i}Q)\tilde{\mathcal{R}}_i}{4\pi\mathcal{R}^2|\partial g/\partial\tau|} \right]_* \mathrm{d}S(y), \tag{2.12}$$

where $[\cdot]_*$ means the values are evaluated at the retarded time $\tau = \tau_* = t - R/a_\infty$. Equation (2.12) is the integral solution to the acoustic analogy that considers the convection effect of oncoming flows. Similar processes in deriving the solution were also employed in several previous aeroacoustic studies (Najafi-Yazdi *et al.* 2011; Ghorbaniasl, Siozos-Rousoulis & Lacor 2016; Zhong & Zhang 2017). For rotor noise, a remaining difficulty is considering the influences of unsteady motions in estimating the retarded time and $|\partial g/\partial\tau|$. In this case, the rotation phase angle ϕ of a point on the blade can be computed as

$$\phi(\tau) = \phi_0 + \int_0^\tau \Omega(s) \,\mathrm{d}s, \tag{2.13}$$

where ϕ_0 is the initial value, and Ω is the time-dependent rotational speed. From (2.4a–c), the temporal derivative of $y_2 = \eta \cos\phi(\tau)$ with respect to τ is

$$\frac{\partial y_2}{\partial\tau} = -\eta \sin\phi \frac{\partial}{\partial\tau}\left[\phi_0 + \int_0^\tau \Omega(s)\,\mathrm{d}s\right] = -\Omega\eta\sin\phi(\tau) = -\Omega y_3. \tag{2.14}$$

Similarly, we have $\partial y_3/\partial\tau = \Omega y_2$. Then, $|\partial g/\partial\tau|$ is evaluated as

$$\left|\frac{\partial g}{\partial\tau}\right| = 1 + \frac{1}{a_\infty}\frac{\partial R}{\partial y_i}\frac{\partial y_i}{\partial\tau} = 1 + \frac{1}{a_\infty}\left[\tilde{R}_1 v_1 - \Omega(\tilde{R}_2 y_3 - \tilde{R}_3 y_2)\right], \tag{2.15}$$

where $v_1(\tau)$ is the vibration speed of the blade in the axial direction, and the effects of unsteady motion are explicitly written as functions of Ω and the local coordinates y_2 and y_3, making it easy to evaluate the impact of each factor on noise radiation.
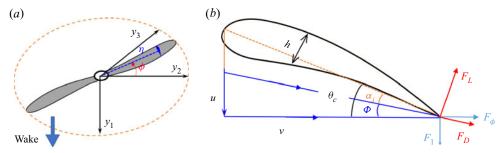
Figure 2. An illustration of the variables for rotor noise source estimation. (*a*) Rotor coordinate system. (*b*) Variables on a section.

There are several differences between (2.12) and the widely used Farassat formulation 1A (Farassat & Succi 1980). First, the convected wave equation accounts for the convection effect of oncoming flows. Second, the temporal derivative to the observer time *t* is kept in (2.12) to simplify the overall computation. Third, the term $1/|\partial g/\partial \tau|$ corresponding to the Doppler effect is explicitly expressed in the source coordinates, making it convenient to account for the impact of non-uniform rotational speed and blade vibration. A remark on the numerical implementation considering the challenges due to unsteady motions is given in Appendix A.

2.2. *Estimating the source terms*

Section 2.1 presents the mathematical framework of rotor noise computation with the effects of unsteady motions incorporated. To compute the rotor noise, we need to evaluate *Q* and L_i at each surface point. An approach to computing the flow variables is to use high-fidelity numerical simulations, which, however, are too expensive for the parametric study of the influential factors. Nevertheless, in this work, CAA simulations will also be conducted for validation.

A reduced-order approach to computing the rotor noise source is the mean surface method (Hanson & Parzych 1993; Zhong *et al.* 2020). An illustration of the coordinate system and blade section elements is presented in figure 2. The rotor blade (the phase angle is ϕ) is divided into various small segments in the radial direction, and the width is dη. At each section, we assume the flow is two-dimensional, and the axial and azimuthal velocities are *u* and *v*, respectively. Here, *u* contains the inflow projection and induced flow in the axial direction and *v* contains inflow projection, blade rotation and induced flow in the tangential direction. Then, the term $Q\,\mathrm{d}S$ in (2.12) can be estimated as

$$Q\,\mathrm{d}S = \rho_\infty \boldsymbol{u} \cdot \boldsymbol{n}\,\mathrm{d}S. \tag{2.16}$$

In the mean surface method (Hanson & Parzych 1993; Zhong *et al.* 2020), the projection of $\boldsymbol{u}$ on the normal vector $\boldsymbol{n}$ is linked to the local pitch angle θ_c and thickness *h* as

$$Q\,\mathrm{d}S = \rho_\infty [u \sin \theta_c + v \cos \theta_c]\,\mathrm{d}\eta\,\mathrm{d}h, \tag{2.17}$$

where d*h* is the variation of blade thickness in the chord direction.

The aerodynamic loading acting on the blade surface will contribute to L_i. For each section shown in figure 2, the forces per unit area in the axial and azimuthal directions are

denoted as F_1 and F_ϕ, respectively. The projections in the y-coordinate are

$$L_1 = -F_1, \quad L_2 = \zeta F_\phi \sin \phi, \quad L_3 = -\zeta F_\phi \cos \phi, \quad (2.18a\text{–}c)$$

where $\zeta = 1$ if the blade rotates in the anti-clockwise direction and $\zeta = -1$ otherwise. As shown in figure 2, the angle of total velocity with the rotation plane is denoted as Φ. Then the equivalent angle of attack α_i is computed as

$$\alpha_i = \theta_c - \Phi. \quad (2.19)$$

Under the assumption that the sectional flow is two-dimensional, at the given α_i and Reynolds number (based on the velocity and chord length), the lift and drag are computed as

$$F_L = \frac{\rho_\infty(u^2 + v^2)}{2} C_L, \quad F_D = \frac{\rho_\infty(u^2 + v^2)}{2} C_D, \quad (2.20a,b)$$

where C_L and C_D are the lift and drag coefficients. As shown in figure 2(b), F_L and F_D are perpendicular and parallel to the total velocity that has an angle of Φ to the rotational plane. Then the force projections in the axial and azimuthal directions are

$$F_1 = \frac{\rho_\infty(u^2 + v^2)}{2}(C_D \sin \Phi - C_L \cos \Phi), \quad F_\phi = \frac{\rho_\infty(u^2 + v^2)}{2}(C_L \sin \Phi + C_D \cos \Phi),$$
$$(2.21a,b)$$

which are substituted to (2.18a–c) to estimate L_i, and $L_i \mathrm{d}S$ is computed as

$$L_i \,\mathrm{d}S \approx L_i c \,\mathrm{d}\eta, \quad (2.22)$$

where c is the chord length.

2.3. *Incorporating the effects of unsteady motions and uncertainty factors*

For a parametric study of unsteady motions and uncertainty factors on rotor noise, we use a cost-effective method based on the blade element moment theory (BEMT) to obtain the aerodynamic variables for source modelling. At a given working state, the sectional flow velocity u, lift and drag coefficients C_L and C_D and therefore the sources based on using (2.17) and (2.22) can be computed. Therefore, the surface integrations in (2.12) are replaced by line integrations. This compact formulation is valid for slender surfaces such as rotors (Bernardini, Gennaretti & Testa 2016; Lopes 2017). The same approach was employed in our previous study of the frequency-domain formation of rotor noise computation (Zhong *et al.* 2020).

However, it is still challenging to consider the unsteady aerodynamic effects in BEMT because of the possible random and complex motions. Fortunately, for practical problems, the amplitudes of these unsteadinesses are often small compared with the mean values. Therefore, we assume the lift coefficient C_L and drag coefficient C_D of the sectional airfoil are the same as in ideal operations. A justification of this assumption is made in the next section using CAA. However, fluctuations in both u and v can still lead to perturbations in the source terms Q and L_i. The term $|\partial g / \partial \tau|$ is also altered. In the future, the effects of unsteady velocity on aerodynamic properties (Van der Wall & Leishman 1994) can also be considered in the model.

More specifically, in this work, we mainly focus on the rotor operations without oblique flow, i.e. the oncoming flow at the speed of $u_\infty = |u_\infty|$ is aligned with the rotor axis.

The target rotational speed is Ω_0, and the chord length at each radial location (denoted as η) is c_0. To describe the unsteady motion, we denote the actual rotation speed as

$$\Omega(\tau) = \Omega_0[1 + \varepsilon_0 + \varepsilon_1(\tau)], \tag{2.23}$$

where ε_0 is a parameter describing the relative deviation of the actual rotation speed Ω from the target value Ω_0, and ε_1 describes the temporal variations. In this case, the actual velocity in the tangential direction is

$$v(\tau) = \Omega(\tau)\eta = \Omega_0\eta[1 + \varepsilon_0 + \varepsilon_1(\tau)]. \tag{2.24}$$

Similarly, if the blade is vibrating, we introduce the parameter ε_2 to quantify the corresponding velocity fluctuation in the axial direction as

$$u(\tau) = u_0 + \varepsilon_2(\tau)v_0 = u_\infty + u_* + \Omega_0\eta\varepsilon_2(\tau), \tag{2.25}$$

where u_* is the induced velocity by the rotor, and it can be computed by using BEMT. As for the geometry asymmetry, in this work, we focus on the possible chord variation

$$c(\eta) = c_0(\eta)[1 + \varepsilon_3(\eta)], \quad \Rightarrow \quad \mathrm{d}S = [1 + \varepsilon_3]c_0\,\mathrm{d}\eta. \tag{2.26}$$

The parameter ε_3 is time invariant but may vary with the radial location. In practice, other factors such as pitch angle variation and section geometry difference can also cause asymmetry. However, the description and following analysis will be similar and are, therefore, not repeated. In this work, we assume the amplitudes of these unsteady motions and uncertainty factors are small, i.e.

$$|\varepsilon_0|, \ |\varepsilon_1|, \ |\varepsilon_2|, \ |\varepsilon_3| \ll 1. \tag{2.27}$$

3. Influences on the aeroacoustics of an isolated rotor

This section will present the parametric study of influences of various unsteadiness and uncertainty factors on the rotor noise. Before that, justification, verification and validation of the noise computation model in § 2 will be presented.

3.1. *Verification of the noise computation model implementation*

First, we will verify the implementation of the noise computation model by comparing results with experimental measurements in an anechoic chamber (Yi *et al.* 2021; Wu *et al.* 2020). The two-bladed rotors APC 9×5 (with the tip radius of $r_{tip} = 11.43$ cm) and APC 11×5 (with the tip radius of $r_{tip} = 13.97$ cm) are investigated. The sectional profile of both blades is close to the NACA4412 airfoil, and the chord and pitch angle distributions in the radial directions are shown in figure 3. Ten microphones at a distance of 1.5 m from the rotor centres are used, and the equivalent observer angle ranges from $\theta = 55°$ to $118°$. In experiments, both rotors are operated at various revolutions per second (RPS). However, there are inevitable deviations and fluctuations in the rotation speeds, which are measured using an optical encoder, and the results are shown in figure 4. The averaged values are kept relatively stable when the speeds are increased after a short time interval. The sampling frequency for RPS measurement is 50 Hz. The unsteadiness quantified by $\varepsilon_1 = (\mathrm{RPS} - \mathrm{RPS}_0)/\mathrm{RPS}_0$, where RPS_0 is the target/nominal rotation speed, is shown in figure 4(*b*), and the amplitude is within ± 0.01.

In the rotor noise prediction model, constant RPS with the averaged values RPS_0 shown in figure 4 and fluctuated RPS are employed as input. For the fluctuated RPS, random
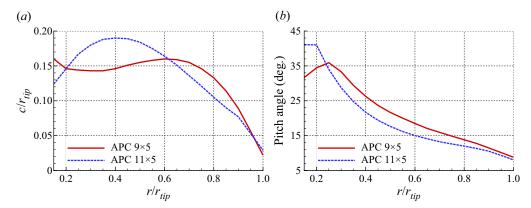
Figure 3. Chord and pitch angle distributions of the two tested APC blades in the radial directions. (*a*) Chord distribution, (*b*) pitch angle distribution.
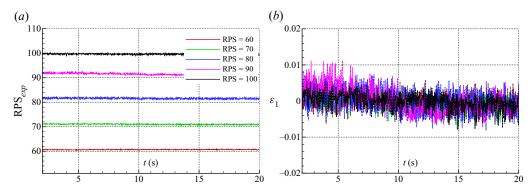

Figure 4. Examples of the measured RPS of a rotor at different target rotation speeds. (*a*) Measured RPS, (*b*) relative error ε_1.

fluctuations with the amplitude of 0.01RPS_0 are added to the averaged value at each time step. In the experiments, it is found that the sound pressure level (SPL) at the blade passing frequency (BPF), which is equal to $2 \times \text{RPS}_0$ for the two-bladed rotors, is often insensitive to the unsteady fluctuations. To this end, in figure 5, we compare the predicted SPL result at different observers with the experimental measurements, showing a close agreement. However, the sampling frequency of the RPS measurements in experiments is only 50 Hz, and variations at high rates are not captured. Therefore, predictions using the fluctuated RPS cannot reproduce the impact of rotation speed unsteadiness on the sound radiation at high frequency. Nevertheless, the close results at the BPF by different approaches, i.e. experiments, constant RPS and fluctuated RPS predictions, suggested the implementation of the prediction model outlined in § 2 is well verified.

3.2. *Validation using CAA*

We also conduct CAA simulations for the APC 9×5 rotor with unsteady rotation speeds to validate the prediction model and justify some assumptions taken in § 2.3. The acoustic preserved artificial compressibility equations suitable for low Mach number aeroacoustic simulations were implemented using an open-source library (Jiang & Zhang 2022). The time marching is realised using a low-dissipation and low-dispersion Runge–Kutta scheme
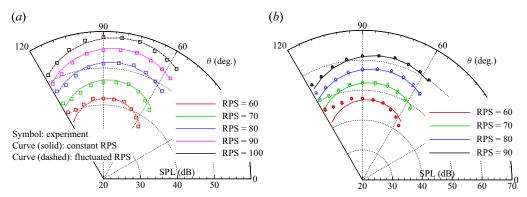
Figure 5. Comparisons of the predicted SPL of the tonal noise at BPF with experiments; (*a*) APC 9×5, (*b*) APC 11×5.

(Hu, Hussaini & Manthey 1996). In the near field, locally orthogonal grids are employed to resolve flow evolution and noise generation. The overall mesh consists of around 15×10^6 cells in the computational domain. The accuracy of the CAA solver for rotor noise simulation has been validated by comparing the predictions with experimental test results (Jiang & Zhang 2022; Jiang *et al.* 2022). In the study, $\text{RPS}_0 = 90$ and the actual RPS is configured as

$$\text{RPS} = \text{RPS}_0[1 + \varepsilon_1 \cos(2\pi \tilde{f} t)], \quad \text{where } \varepsilon_1 = 0.01, \ \tilde{f} = 10 \times \text{RPS}_0. \tag{3.1}$$

The unsteady thrust predicted by the CAA simulation is shown in figure 6(*a*). The time-averaged thrust is $T_0 \approx 2.62\,\text{N}$, which is close to the steady rotor simulation result using CAA. The thrust prediction by BEMT is approximately $2.6\,\text{N}$. In § 2.3, we assume that C_L and C_D are unchanged in the presence of the unsteady motion, which should be examined using the CAA results. For simplicity, we denote the thrust coefficient for the steady rotor as C_0, i.e. $T_0 = C_0 \Omega_0^2$, where $\Omega_0 = 2\pi \times \text{RPS}_0$. The thrust coefficient of the unsteady rotor is denoted as C such that

$$T(t) = C\Omega^2 = C\Omega_0^2[1 + \varepsilon_1 \cos(2\pi \tilde{f} t)]^2 \approx T_0 \frac{C}{C_0}[1 + 2\varepsilon_1 \cos(2\pi \tilde{f} t)], \tag{3.2}$$

where $\Omega = 2\pi \times \text{RPS}$. Then, we perform Fourier transform of $T(t)$ (normalised by T_0) obtained by CAA, and the result is shown in figure 6(*b*). At $f/\text{RPS}_0 = 10$, the amplitude of the normalised spectrum is close to $2\varepsilon_1$, as indicated by the red dot, suggesting that $C/C_0 \approx 1$, i.e. the thrust coefficient remains unchanged. Therefore, the assumption of constant C_L and C_D employed in the prediction model is indirectly justified.

In the numerical simulation, sound pressures at different observer points are also obtained and compared with the prediction results. Figure 7 shows the comparisons of noise spectra at $r_o = 0.2\,\text{m}$ and $0.4\,\text{m}$. Both observers have the same observer angle of $\theta = 90°$, but the spectra are quite different because they are located in the near field. At BPF and its harmonics, the predicted SPLs are close to the high-fidelity CAA simulation. The computation times for the prediction model and high-fidelity CAA are a few seconds and more than 24 h, respectively. However, the broadband noise, mainly caused by the turbulence interaction at both the leading edge and trailing edge of the blades, is not contained in the prediction model.
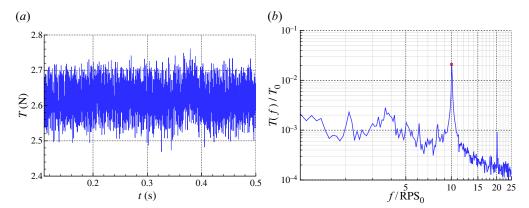
Figure 6. The computed time signal and spectrum of the rotor with fluctuated rotation speed using high-fidelity CAA simulation. For this case, $RPS_0 = 90$. (*a*) Thrust signal, (*b*) thrust spectrum (scaled by T_0).
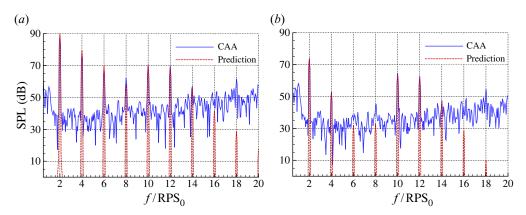

Figure 7. Comparisons of the predicted SPL spectra with high-fidelity CAA simulations at $\theta = 90°$ and different observer distances r_o. For this case, $RPS_0 = 90$; (*a*) $r_o = 0.2$ m, (*b*) $r_o = 0.4$ m.

3.3. *Influence of rotation speed variation*

In the following, we will conduct a parametric study of the unsteady motion and uncertainty factors based on the two-bladed rotor APC 9×5, i.e. the blade number $B = 2$, in the hover state. The target rotation speed is $RPS_0 = 100$. The observer distance is set as $r_o = 1.5$ m $\approx 13r_{tip}$, where r_{tip} is the rotor radius.

In this section, we study the influence of rotation speed variation using the proposed time-domain formulations in § 2. The additional source strengths of ΔQ, ΔF_L and ΔF_D are linearly dependent on the parameters ε_0 and ε_1. However, the variation of ε_1 also influences the estimated retarded time and the associated time derivatives, affecting the sound in a wide frequency range. In this section, we rewrite the relative difference between Ω_0 and Ω defined in (2.23) as

$$\varepsilon_0 + \varepsilon_1(\tau) = \varepsilon_0 + \sum A_n \cos(2\pi f_n \tau + \gamma_n) + \varepsilon_1^*(\tau), \tag{3.3}$$

where ε_0 means the static deviation, and ε_1 and ε_1^* describe the periodic and random fluctuations.
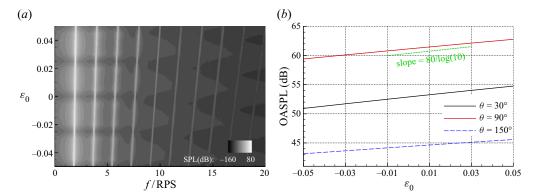
956 A16-12

(*a*)

(*b*)

Figure 8. The influence of the static deviation of the rotational speed; (*a*) spectra, (*b*) OASPL.

3.3.1. *Static deviation of rotation speed*

If the uncertainty factor in the rotation speed only contains the static deviation ε_0, the actual rotation angular frequency Ω has a deviation from the target value of Ω_0. One consequence is that the BPF has a variation of $\varepsilon_0 \times$ BPF. The effect is shown in figure 8(*a*), where the frequency of each harmonic of BPF varies with ε_0 linearly. Moreover, in this case, the noise is dominated by the tonal noise at the BPF. The varied rotation speed can alter the strength of noise emission, and the acoustic scaling law (Zhong *et al.* 2020) suggests the sound pressure amplitudes have a dependence of $(\Omega/\Omega_0)^h$, i.e. the difference in the SPL is

$$\Delta \mathrm{SPL} = 20 \log_{10} \left(\frac{\Omega}{\Omega_0} \right)^h = 20h \log_{10}(1 + \varepsilon_0) \approx \frac{20h}{\log 10} \varepsilon_0. \tag{3.4}$$

The coefficient h is dependent on the order of the BPF harmonics and observer angle (Zhong *et al.* 2020). The dependence of the overall sound pressure level (OASPL) computed in the frequency range of 50–5000 Hz with ε_0 at different observers is shown in figure 8(*b*). At $\theta = 90°$, the coefficient is $h = B + 2 = 4$ for the tone at BPF, which is a significant contribution to sound if the steady aerodynamic forces are considered. By contrast, at $\theta = 30°$ and $\theta = 150°$, the noise at BPF is less significant while the contributions by tones at higher frequencies, which have other dependencies on Ω, are increased, leading to different slopes. In the figure, the low noise levels at -160 dB, i.e. the sound pressure amplitudes tend to 0, are presented, which, however, might be covered by other noise components in practice.

For a single rotor, when ε_0 is small, e.g. $|\varepsilon_0| < 0.01$, the influence on the SPL is negligible. The difference in the peak location is distinguishable due to the finite frequency resolution. However, it does not mean that the RPS deviation effect is unimportant. For example, in dual rotor applications, the difference in the rotation speed can lead to a varying phase difference between the rotating blades, altering the interference effect of the sound waves. The effect will be investigated in § 4.

3.3.2. *Periodic fluctuation of rotation speed*

In this section, we consider cases such that the rotational speed fluctuation is periodic, i.e. the influence of sinusoidal terms in (3.3) is studied. The frequency of the RPS fluctuation is f_n, and it is not necessarily a harmonic of BPF as in the frequency-domain solver (Hanson & Parzych 1993; Zhong *et al.* 2020).
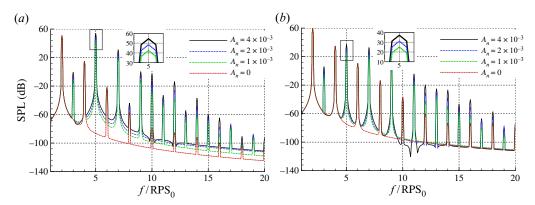
Figure 9. Computed rotor noise spectra at different observers if there are periodic fluctuations in the rotation speed. The frequency of periodic fluctuation is $f_n = 500\,\mathrm{Hz}$; (a) $\theta = 30°$, (b) $\theta = 90°$.

Figure 9 shows the acoustic spectra with $f_n = 500\,\mathrm{Hz}$ (i.e. $5 \times \mathrm{RPS}_0$) at $\theta = 30°$ and 90°, respectively. When $A_n = 0$, which means the rotation has a constant speed, tonal noise is produced at the $\mathrm{BPF} = 2 \times \mathrm{RPS}_0$ and its harmonics. However, the SPL is rapidly reduced with the increase of harmonic number. For example, the SPL at $2 \times \mathrm{BPF}$ is lower than that at BPF by approximately 40 dB. By contrast, if there is a slight variation in the rotation speed, e.g. for cases with $A_n = 1 \times 10^{-3}$, 2×10^{-3} and 4×10^{-3}, additional tonal noise is produced at f_n, and the SPL is comparable to that at BPF. Multiple peaks are also found at other frequencies of $f_n + k \times \mathrm{RPS}_0$, where k is an integer. As shown in the zoomed regions in figure 9, at $f = f_n$, the SPL increases by approximately 6 dB when A_n is doubled, suggesting that the magnitude of produced sound is proportional to the periodic fluctuation amplitude A_n. It should be emphasised that the extra tones at the harmonics of RPS_0 cannot be captured by the frequency-domain method (Hanson & Parzych 1993; Zhong *et al.* 2020).

To further consider how the periodic unsteady motion affects the additional tonal noise components, we investigate the two close frequencies of $f_n = 1200\,\mathrm{Hz}$ and 1230 Hz. The computed noise spectra at $\theta = 90°$ are shown in figure 10. When $f_n = 1200\,\mathrm{Hz}$, which is an integer multiple of the BPF, the noise peaks in the high-frequency range only appear at the harmonics of the BPF. By contrast, as shown in figure 10(b), when $f_n = 1230\,\mathrm{Hz}$, amplitudes of the tonal noise at the harmonics of BPF are unchanged. There are significant tones at $(12.3 + 2k) \times \mathrm{RPS}_0$, where k is an integer. Also, the amplitudes of those tones are close to those at $(12 + 2k) \times \mathrm{RPS}_0$ in figure 10(a). There are several slight peaks with a difference of $\pm 0.3 \times \mathrm{RPS}_0$ from the main peaks. The results suggest that the periodic motions can produce significant tones related to both f_n, the frequency of the RPS fluctuation, and the mean rotation speed RPS_0.

To better understand the dependence of noise features on the frequency of the periodic motion, we compute the sound radiation with the parameter f_n ranging from 0 to 1600 Hz. The mean rotation speed is $\mathrm{RPS}_0 = 100$. The corresponding acoustic spectra are computed, and the results at $\theta = 30°$ and 90° are shown in figure 11. For different f_n, the peak values are always high at the BPF and its harmonics, which are likely contributed to by the mean rotation speed. Besides, there are high levels of sound at the frequency of $f = f_n$, and there are relatively low but discernible peaks at the alternative frequencies of $f = f_n \pm l \times \mathrm{BPF}$, where l is an integer. In figure 10(b), there are also peaks at the frequencies that seem to be the combination of the BPF and f_n, although the levels are
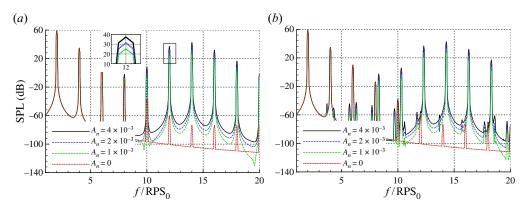
956 A16-14

Figure 10. Computed spectra of the rotor noise at $\theta = 90°$. There are periodic fluctuations with different f_n in the rotation speed; (*a*) $f_n = 1200$ Hz, (*b*) $f_n = 1230$ Hz.
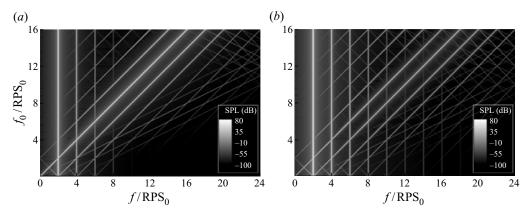

Figure 11. Computed spectra of a two-bladed rotor with periodic fluctuation in RPS. The amplitude of the periodic fluctuations is $A_n = 2 \times 10^{-3}$, and f_n ranges from 0 to 1600 Hz; (*a*) $\theta = 30°$, (*b*) $\theta = 90°$.

relatively low. Figure 11 shows that there is a complex dependence of the observed peak locations on f_n, especially when f_n is high. By contrast, at low perturbation frequency, e.g. $f_n < 2 \times \mathrm{RPS}_0$, the periodic motion only produces several peaks at low frequencies, and the influence on the tonal noise at high frequencies is relatively unimportant. At $\theta = 90°$, clear tones are produced at high f_n. The results suggest that the periodic motion can equivalently produce an additional sound source at f_n, which is then modulated by the rotational motion of the blade at RPS_0.

The investigation of the acoustic spectra suggested that the periodic fluctuation of the rotation speed can produce additional tonal noise. The locations of the peaks are sensitive to f_n and are related to RPS_0. Figure 9 shows that, if additional peaks are produced due to the periodic motion, the amplitudes of the sound pressure are likely proportional to the amplitude A_n. However, the noise due to the overall aerodynamic force due to the rotation is also significant, especially at BPF. To this end, in this work, we consider the extra acoustic energy estimated by integrating the sound power from 50 to 5000 Hz, due to the unsteady periodic fluctuation. The dependence of the extra sound energy on f_n and A_n^2 is shown in figure 12. In the results, A_n^2 indicates the amplitude of the equivalent sound source that is likely proportional to the amplitude of the unsteady fluctuation. The values
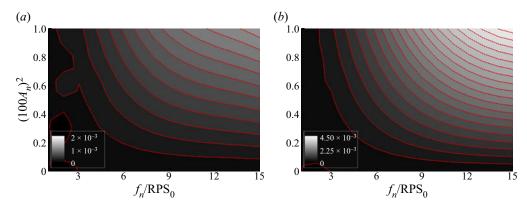
956 A16-15

Figure 12. The dependence of additional acoustic energy ΔE on f_n and A_n of the periodically fluctuated rotation speed at different observer angles; (a) $\theta = 30°$, (b) $\theta = 90°$.
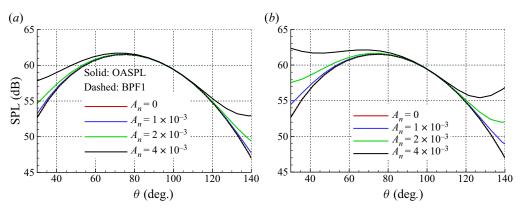

Figure 13. A comparison of directivities with rotation speed variations at different f_n; (a) $f_n = 500$ Hz, (b) $f_n = 1200$ Hz.

are multiplied by 100 for convenience. When f_n is relatively high, e.g. $f_n > 9 \times \mathrm{RPS}_0$, a relatively even increase of ΔE with A_n^2 is achieved, suggesting that the strength of the extra sound pressure is dependent on A_n linearly. By contrast, at low f_n, there is a lower increase of ΔE with the same A_n^2. Moreover, the amplitudes of the extra acoustic energy at $\theta = 90°$ are much lower than that at $\theta = 30°$.

The acoustic directivity of the SPL at BPF, and the OASPL (calculated from 50 to 5000 Hz) with $f_n = 500$ Hz and 1200 Hz, respectively, is computed. The observer angles range from $\theta = 30°$ to $150°$, and the amplitudes of $A_n = 1 \times 10^{-3}, 2 \times 10^{-3}$ and 4×10^{-3} are considered. The results are shown in figure 13. At both frequencies, little difference is found at $\theta = 90°$ for different A_n. The reason is that the original noise level at the BPF is relatively high; meanwhile, the extra acoustic energy due to the unsteady factor is relatively low, slightly changing the noise level. By contrast, the unsteady effect is more profound in the upstream and downstream directions, while the original levels at the corresponding locations are low, leading to a significant increase.

3.3.3. *Random fluctuation of rotation speed*

This section studies the influence of random fluctuations in the actual RPS, described by the term ε_1^* in (3.3). In experiments, determining the property of ε_1^* is difficult as a high
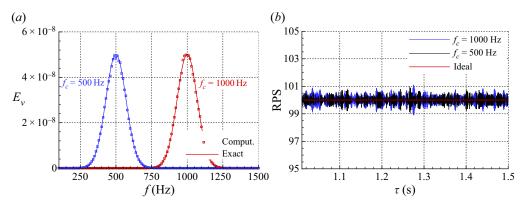
(a)

(b)

Figure 14. The spectra of the random fluctuations denoted by ε_1^* in the rotation speed and the synthesised time signals. (a) Spectra, (b) time signals.

sampling frequency is needed to obtain the instantaneous rotation speed. Therefore, we assume that the inevitable random fluctuations (see figure 4) have power spectral density (PSD) with Gaussian distributions

$$E_1^*(f) = A_G \exp[-\Lambda_A(f - f_c)^2], \tag{3.5}$$

where f is the frequency, A_G is the amplitude and Λ_A and f_c control the shape of the spectrum. In this work, $\Lambda_A = 10^{-4}$ is studied without loss of generality. Figure 14(a) shows the two spectra with $f_c = 500$ Hz and $f_c = 1000$ Hz with $A_G = 5 \times 10^{-8}$. The spectra in the frequency domain are realised as randomly varying time signals $\varepsilon_1^*(t)$ shown in figure 14(b), based on which we recomputed the PSD, and the results reproduce the target spectra satisfactorily, as indicated by the dots in figure 14(a). With the time signals of $\varepsilon_1^*(t)$, we can compute the corresponding fluctuations in RPS. The fluctuating rotational speed is within 1 % of RPS_0.

Using the formulations outlined in § 2, we are able to compute the noise spectra with randomly fluctuated RPS. Figure 15 shows the results with A_G ranging from 0.5×10^{-8} to 5×10^{-8}. The observer angles are $\theta = 30°$ and $90°$, and the results are compared with those with steady rotational speed (red dashed curves). The random fluctuations can lead to broadband-type noise features, while the tonal noise at BPF is slightly altered. The noise level due to the RPS fluctuation is much higher than the tonal noise peaks in a wide frequency range. At $\theta = 90°$, the tonal noise at $2 \times$ BPF is relatively high, and values are not altered by the random RPS fluctuations either. Furthermore, there are maximum values of a bump-shaped spectrum around $f_c = 500$ Hz, relating to the PSD of ε_1^*. However, the bump shapes are observer angle dependent.

As indicated by arrows in figure 15, the levels of the humps increase with A_G. In this work, we extract the broadband noise spectra linked to the randomly perturbed RPS by using a robust locally weighted regression method (Cleveland 1979). Moreover, the results due to different A_G are scaled to that of $A_{G0} = 0.5 \times 10^{-8}$, i.e. we define a new variable of $\text{SPL}^* = \text{SPL} - 10\log_{10}(A_G/A_{G0})$, and the results are shown in figure 16. The humped peaks are collapsed around $f_c = 500$ Hz and 1000 Hz, respectively, suggesting the strengths of the equivalent broadband noise sources are proportional to A_G. In addition, the results are close for $\theta = 30°$ and $150°$, and they are higher than that at $\theta = 90°$.
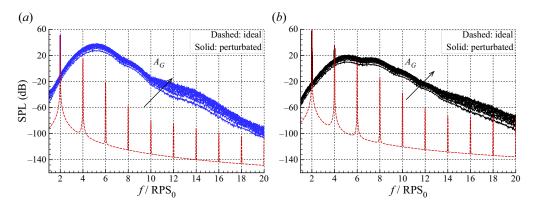
956 A16-17

Figure 15. Computed noise spectra with random fluctuations in RPS. The fluctuations have Gaussian distributions, and $f_c = 500\,\mathrm{Hz}$ and A_G ranges from 0.5×10^{-8} to 5×10^{-8}; (a) $\theta = 30°$, (b) $\theta = 90°$.
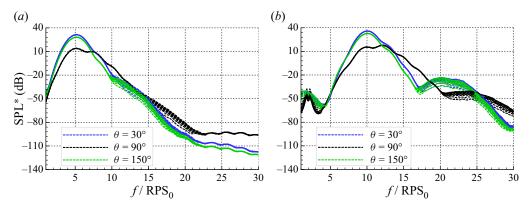

Figure 16. Computed equivalent broadband noise spectra with different random fluctuations in RPS. The SPL is scaled by B_G, the amplitude of the random fluctuations; (a) $f_c = 500\,\mathrm{Hz}$, (b) $f_c = 1000\,\mathrm{Hz}$.

3.4. *Influence of blade vibration*

This section investigates the influence of blade vibration in the axial direction. Equation (2.25) introduces the parameter $\varepsilon_2(t)$ for quantification, which, similarly, can be decomposed into the periodic motion and random fluctuation, i.e.

$$\varepsilon_2(\tau) = \sum B_n \cos(2\pi f_n \tau + \varphi_n) + \varepsilon_2^*(\tau), \tag{3.6}$$

where B_n and f_n are the amplitude and frequency of the periodic motion, respectively, and ε_2^* corresponds to the possible random vibration.

First, the influence of periodic vibrations with $f_n = 100\,\mathrm{Hz}$ and $1000\,\mathrm{Hz}$ on rotor noise is studied. For both cases, the vibration amplitude is assumed as $B_n = 2 \times 10^{-3}$, and the computed spectra results are shown in figure 17. At $\theta = 30°$, for each periodic frequency f_n, peaks are found at $f_n + l \times \mathrm{BPF}$, where the l values are integers. For example, when $f_n = 100\,\mathrm{Hz}$ (the green curves), extra peaks are found at $300\,\mathrm{Hz}$, $500\,\mathrm{Hz}$ and $700\,\mathrm{Hz}$, ..., with decreasing amplitudes. Similarly, when $f_n = 1000\,\mathrm{Hz}$ (the black curves), levels of the tonal noise at $800\,\mathrm{Hz}$, $1000\,\mathrm{Hz}$, $1200\,\mathrm{Hz}$ and $1400\,\mathrm{Hz}$ are significantly increased. However, at $\theta = 90°$, the noise spectra are little affected, being close to that of the steady blade. The results suggest that the blade variation can hardly affect the tonal noise on the rotational
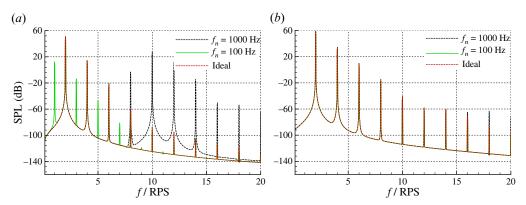
Figure 17. Computed noise spectra at different observers with periodic blade vibrations. Here, $B_n = 2 \times 10^{-3}$ and $f_n = 100\,\mathrm{Hz}$ and $1000\,\mathrm{Hz}$ are studied; (a) $\theta = 30°$, (b) $\theta = 90°$.
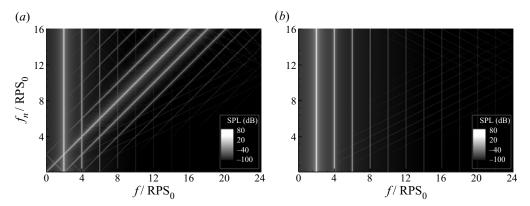

Figure 18. Computed noise spectra at different observer angles with periodic blade vibration. Cases with $B_n = 2 \times 10^{-3}$, and f_n ranges from 0 to 1600 Hz are studied; (a) $\theta = 30°$, (b) $\theta = 90°$.

plane because the blade vibrations can cause pulsating motions in the axial direction, resulting in an equivalent acoustic dipole. This conclusion is also applicable to other f_n. Figure 18 shows the spectra at $\theta = 30°$ and $\theta = 90°$ with f_n ranging from 0 to 1600 Hz. Clear tones at BPF and its harmonics are found at both observer angles. Moreover, at $\theta = 30°$, there are also multiple parallel lines at $f = f_n + l \times$ BPF. At $\theta = 90°$, the tonal noise only occurs at the harmonics of BPF.

The vibration can also be random, as described by ε_2^* in (3.6). In this case, we assume the PSD of the random fluctuation has a Gaussian distribution

$$E_2^*(f) = B_G \exp[-\Lambda_B(f - f_c)^2]. \tag{3.7}$$

In practical applications, time signals of $\varepsilon_2^*(t)$ are realised by using the PSD in the frequency domain with $\Lambda_B = 1 \times 10^{-4}$, $f_c = 500\,\mathrm{Hz}$ and B_G ranges from 0.5×10^{-8} to 5×10^{-8}. A comparison of the resulting noise spectra at different observers is shown in figure 19. Again, the random vibrations do not alter the tonal noise components at the BPF harmonics (if discernible) in the spectra. Instead, they equivalently produce broadband-type spectra, and the noise level increases with B_G. At $\theta = 30°$, the broadband content is bumped shaped with the peak locations around $f = f_c$. At $\theta = 90°$, there are
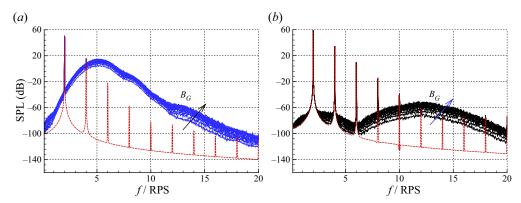
Figure 19. Computed noise spectra at different observers with random blade vibration with a Gaussian distribution. Here, $f_c = 500$ Hz and B_G ranges from 0.5×10^{-8} to 5×10^{-8}; (a) $\theta = 30°$, (b) $\theta = 90°$.
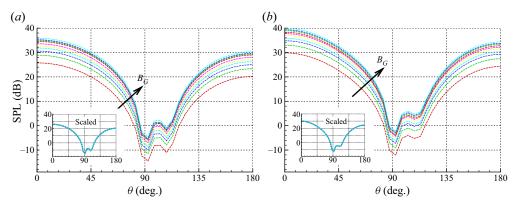

Figure 20. Computed directivity patterns of the equivalent broadband noise due to the random blade vibrations with $f_c = 500$ Hz and 1000 Hz, respectively. Here, B_G ranges from 0.5×10^{-8} to 5×10^{-8}; (a) $f_c = 500$ Hz, (b) $f_c = 1000$ Hz.

also broadband-shaped noise spectra, the amplitudes of which are much lower than that at $\theta = 30°$ (approximately 70 dB). As a result, the peaks of the tonal noise are discernible at that observer angle. In this work, we also compute the OASPL (from 50 to 5000 Hz) of the equivalent components having a random vibration at different observer angles ranging from $\theta = 30°$ to $150°$. The results for $f_c = 500$ Hz and $f_c = 1000$ Hz are shown in figure 20. High noise levels are found in the upstream and downstream directions due to the dipole property of the equivalent noise sources. The SPL data scaled by the amplitude as $\text{SPL}^* = \text{SPL} - 10 \log_{10}(B_G/B_{G0})$ with $B_{G0} = 0.5 \times 10^{-8}$ are shown in the insets in figure 20. The collapsed results suggest the strength of equivalent broadband noise is proportional to the amplitudes of the random vibration. Additionally, levels of the equivalent broadband noise increase with f_c.

3.5. *Influence of geometry asymmetry*

This section investigates the influence of geometry asymmetry on rotor noise emission. For the two-bladed rotor under investigation, we assume the chord of one blade is $c = c_0(1 + \varepsilon_3)$, while the other one remains c_0. In this work, small values of $\varepsilon_3 = 0.01, 0.02$ and 0.04 are investigated. First, we assume the rotor has a constant rotation speed, and
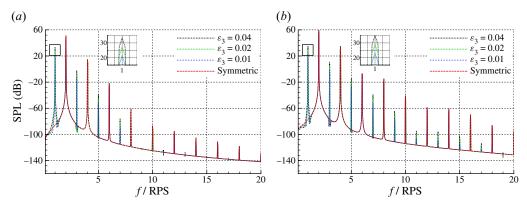
Figure 21. Computed noise spectra of asymmetric blades with constant RPS = RPS_0; (*a*) $\theta = 30°$, (*b*) $\theta = 90°$.

the computed noise spectra at different observer angles are shown in figure 21. Compared with the symmetric rotor, which corresponds to $\varepsilon_3 = 0$, multiple extra peaks are found at $k \times RPS_0 + l \times BPF$ with k and l as integers. Moreover, for those additional peaks, as indicated by the zoomed-in insets in figure 21, a difference of 6 dB is found when ε_3 is doubled. Meanwhile, compared with the symmetric blade, the noise levels of the asymmetric blades at BPF harmonics are nearly unchanged.

Similarly, we can compute the noise spectra of the asymmetrical blades experiencing a periodic unsteady motion as quantified in (3.3). The frequency is $f_n = 1000$ Hz and the amplitude is $A_n = 2 \times 10^{-3}$. The results at different observer angles are shown in figure 22. Due to the periodic fluctuation of the rotation speed, the tonal noise around $10 \times RPS_0$ is increased, as investigated in § 3.3.2. Those peaks are not altered even though the blade geometries are asymmetric. Instead, there are additional tones between the peaks due to the periodically fluctuating rotation speed. The amplitudes of those tones (at $1 \times RPS_0$, $3 \times RPS_0$, $5 \times RPS_0$, ...) are increased by approximately 6 dB when ε_3 is doubled. We can also compute the noise spectra of the asymmetric blade when the rotation speed has random fluctuations. The PSD of the random fluctuation is described in (3.3) with $A_G = 5 \times 10^{-8}$ and $f_c = 500$ Hz. Again, as shown in figure 23, bump-type broadband noise is produced due to the fluctuated rotation speed, which overwhelms most of the tonal noise in the spectra. However, discernible peaks at 100 Hz are found, and the amplitude increases with ε_3, while the noise level at BPF is unchanged.

In this work, the asymmetry is described by introducing variations in the chord. A more generic configuration with spatially dependent ε_3 can be considered as well. Technically, the effects of other uncertainties in pitch angle distribution can also be investigated using the same approach in this section. However, the blade asymmetry can cause mass imbalances in practice, resulting in structural vibration and altering the noise emission feature.

4. Influences on the aeroacoustics of dual rotors

In practical applications, a flying vehicle is often equipped with multiple rotors, and the rotation speed of each rotor is continuously adjusted for flight control. Studies on the aerodynamic noise features of multiple rotors have been conducted (Shukla & Komerath 2018; Alvarez & Ning 2020; Bernardini *et al.* 2020; de Vries *et al.* 2021; Bu, Ma & Zhong 2022). However, the influence of the multi-rotor interaction on noise generation
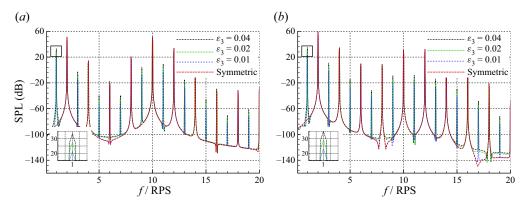
Figure 22. Computed noise spectra of asymmetric blades with periodically fluctuated RPS. The frequency of the periodic motion is $f_n = 1000\,\text{Hz}$ and the amplitude is $A_n = 2 \times 10^{-3}$; (a) $\theta = 30°$, (b) $\theta = 90°$.

is still debated as contradictory conclusions were made in previous studies (Zhou *et al.* 2017; Zhou & Fattah 2017). The numerical studies by Lee & Lee (2020) showed a noise variation of up to 20 dB. By contrast, the experiments by Bu *et al.* (2021) suggested both aerodynamic forces and noise features are insensitive to the separation distances and initial configurations. The observations might be linked to the fact that the dual rotor aeroacoustics have been influenced by unsteady motions and uncertainty factors, which are studied in this section.

In the following study, we assume that the dual rotors, either co-rotating or counter-rotating, have identical geometry and are placed on the same plane. The separation distance of the centres is $1.1D$, where D is the rotor diameter. For this configuration, the effect of mutual interactions of the rotors on the aerodynamic force is regarded as insignificant (Bu *et al.* 2021). Therefore, we assume the sound source generated aerodynamically by each rotor is the same as that of an isolated rotor.

4.1. *Co-rotating dual rotors*

Usually, the sound waves produced by the sources on the rotor blade surface experience different time delays as the source locations vary with the rotation. Therefore, for a dual rotor system, the difference in the initial phase angle $\Delta\phi_0$ of the blades might significantly alter the noise feature. First, we study the co-rotating dual rotors at the constant rotation speed of RPS_0 and $\Delta\phi_0 = 0°$ and $90°$. The resultant noise spectra at different observers quantified by the polar angle θ and azimuthal angle φ (cf. the schematic in figure 1) are shown in figure 24. The results due to a single rotor are also included for comparison. The tonal noise components are only found at the harmonics of BPF, and the amplitudes decrease with frequency because there is no fluctuation in the rotation speed. At $\varphi = 0°$ (on the rotation plane), as shown in figure 24(*a*), the results at both $\Delta\phi_0 = 0°$ and $90°$ are close, and they are slightly higher than those of the single rotor. By contrast, because of the interference effect, the noise level of the $\Delta\phi_0 = 90°$ case is lower than the $\Delta\phi_0 = 0°$ case by 20 dB at $\varphi = 90°$ (on the perpendicular plane). The results suggest that significant noise reduction at particular observers might be achieved via phase control.

Next, we will investigate the influence of rotational speed fluctuations on the sound interference. As described previously, for both $\Delta\phi_0 = 0°$ and $\Delta\phi_0 = 90°$ cases, we assume the rotation speed has a periodic fluctuation at $f_n = 1000\,\text{Hz}$, and the amplitude is $A_n = 10^{-3}$. A comparison of the computed noise spectra at different observer angles
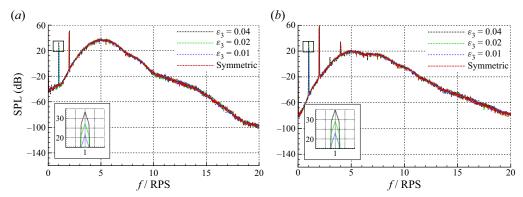
956 A16-22

Figure 23. Computed noise spectra of asymmetric blades with random fluctuations in RPS ($A_G = 5 \times 10^{-8}$ and $f_c = 500\,\text{Hz}$); (a) $\theta = 30°$, (b) $\theta = 90°$.
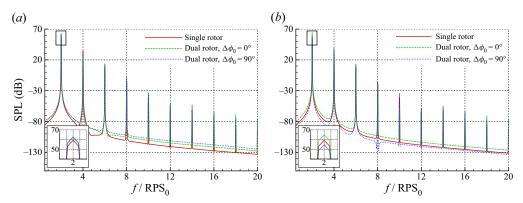

Figure 24. Computed sound spectra of two rotors with identical and constant rotation speeds. The observers are at (a) $\theta = 90°$ and $\varphi = 0°$, (b) $\theta = 90°$ and $\varphi = 90°$.

is shown in figure 25. Consequently, the tonal noise levels in the high-frequency range are increased due to periodic fluctuations. However, the impact of the mechanism of phase difference $\Delta\phi_0$ on the perceived noise is similar to that with constant rotation speed. At $\varphi = 0°$, the noise spectra of both configurations are close; at the observer angle of $\varphi = 90°$, a difference in SPL of up to $10\,\text{dB}$ is found between the $\Delta\phi_0 = 90°$ and $\Delta\phi_0 = 0°$ cases. Ideally, the temporal variation of the rotation speed can yield different phase angle differences of the sources and therefore affect the interference of sound waves. However, the accumulated phase difference remains small if the rotation speed fluctuation is periodic and the amplitude $A_n \ll 1$. More importantly, the frequency of the periodic fluctuation is high, making the actual variation in $\Delta\phi$ due to unsteady motion negligible. In other words, $\Delta\phi(t) \approx \Delta\phi_0$ and the effect of phase delay on the acoustic interference is the same as in the cases with constant rotation speeds. A comparison of the time signals at different observers is shown in figure 26. Again, this shows that the difference in the results at $\varphi = 0°$ is relatively small, while destructive superposition makes the acoustic amplitudes very small at $\varphi = 90°$ if $\Delta\phi_0 = 90°$.

However, if there is a slight difference in the mean rotation speeds $\text{RPS}_0^{(1)}$ and $\text{RPS}_0^{(2)}$ due to the static deviations described by ε_0, the phase difference $\Delta\phi$ will vary with time. As a result, the interference effect due to $\Delta\phi_0$ is likely unimportant. To examine
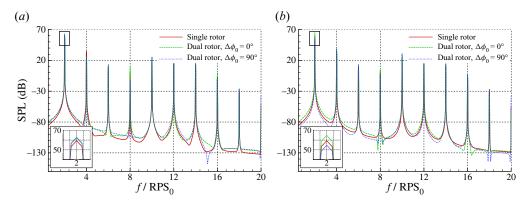
956 A16-23

Figure 25. Computed sound spectra of two rotors with periodic fluctuations in RPS with $f_n = 1000$ Hz and $A_n = 10^{-3}$. The observers are at (a) $\theta = 90°$ and $\varphi = 0°$, (b) $\theta = 90°$ and $\varphi = 90°$.
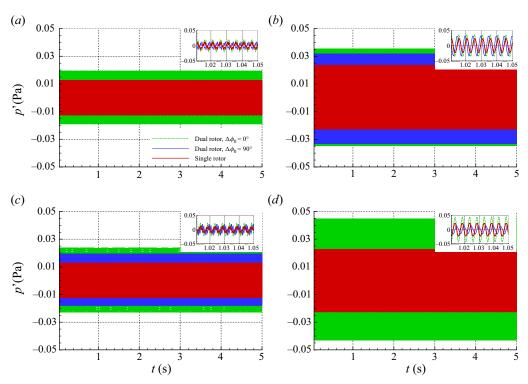

Figure 26. Computed time signals of two rotors with periodic fluctuations in RPS with $f_n = 1000$ Hz and $A_n = 10^{-3}$; (a) $\theta = 30°$ and $\varphi = 0°$, (b) $\theta = 90°$ and $\varphi = 0°$, (c) $\theta = 30°$ and $\varphi = 90°$, (d) $\theta = 90°$ and $\varphi = 90°$.

this conjecture, we conducted computations with $RPS_0^{(1)} = 99.5$ and $RPS_0^{(2)} = 100.5$ and compare the results for $\Delta\phi_0 = 0°$ and $90°$, respectively. Moreover, we assume the actual RPS has periodic fluctuations with $f_n = 1000$ Hz and $A_n = 10^{-3}$. The computed sound spectra at $\varphi = 0°$ and $90°$ (and the polar angle is $\theta = 90°$ for both cases) are shown in figure 27. Compared with the single rotor, the noise spectra in the dual rotor configuration are higher, but both results for $\Delta\phi_0 = 0°$ and $\Delta\phi_0 = 90°$ are close, as expected.
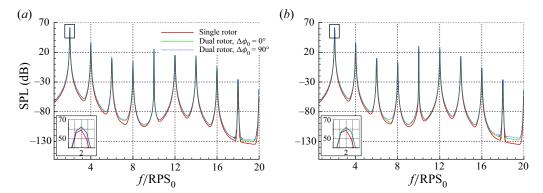
956 A16-24

Figure 27. Computed sound spectra of two rotors with slight difference in RPS_0. The actual RPS is perturbed with periodic fluctuations (with $f_n = 1000\,\mathrm{Hz}$ and $A_n = 10^{-3}$); (*a*) $\theta = 90°$ and $\varphi = 0°$, (*b*) $\theta = 90°$ and $\varphi = 90°$.

In addition, unlike the results shown in figure 25, the difference in the results at different azimuthal angles is small.

Apart from the periodic fluctuation, we can also study the influence of random fluctuations in the rotation speed. Figure 28 shows the noise spectra with $f_c = 500\,\mathrm{Hz}$ and $A_G = 0.5 \times 10^{-8}$. Again, the random fluctuations produce bump-type broadband spectra, and some tonal noise is overwhelmed. However, at high frequencies, i.e. $f \geq 10 \times RPS_0$, the peaks are observed again as their levels are higher than the broadband contents. The results with different $\Delta\phi_0$ are close, and the tones at the BPF are nearly unchanged. Meanwhile, the results of both dual rotor configurations are approximately 3 dB higher than that of the single rotor, similar to the experimental observations (Bu *et al.* 2021). Figure 29 shows comparisons of the time signals of different configurations at different observers in the presence of deviations and unsteady fluctuations in the rotation speed variation. At $\theta = 30°$ (downstream), stochastic signals are seen as the random fluctuations of rotation speed that can lead to profound broadband noise contents. For both dual rotor configurations, clusters of sound signals occasionally appear, suggesting that wave packets are formed due to the slight difference in the mean rotation speeds. The phenomenon is more apparent at $\theta = 90°$, and the frequency of the wave packet is approximately 1 Hz, which is the rotation speed difference between the rotors. Consequently, the amplitudes of the sound signals are close despite the phase differences of the wave packets, explaining why the spectra are comparable.

4.2. *Counter-rotating dual rotors*

We can also study the influence of the counter-rotating dual rotors. In this case, when computing the loadings using (2.18*a–c*), the value of ζ is taken as $+1$ and -1 for anti-clockwise and clockwise rotating blades, respectively. The rotation direction will affect the source locations and the projections of aerodynamic loading in different directions. Firstly, we assume the averaged rotation speeds of both rotors are $RPS_0 = 100$, on top of which there are periodic fluctuations with $A_n = 10^{-3}$ and $f_n = 500\,\mathrm{Hz}$. The initial phase difference is $\Delta\phi_0 = 45°$. Computations are also conducted for the co-rotating dual rotors for comparison. Figure 30 shows the computed spectra at azimuthal observers of $\varphi = 0°$ and $90°$, respectively. The polar angle for both observers is $\theta = 90°$. At $\varphi = 0°$, the results for both co-rotating and counter-rotating configurations are close at BPF.
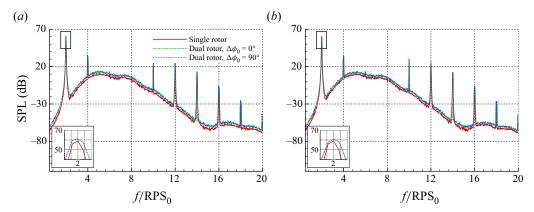
956 A16-25

Figure 28. Computed sound spectra of two rotors with slight difference in RPS_0 of 99.5 and 100.5. The actual RPS is perturbed with periodic (with $f_n = 1000\,\text{Hz}$ and $A_n = 10^{-3}$) and random (with $f_c = 500\,\text{Hz}$ and $A_G = 0.5 \times 10^{-8}$) fluctuations; (a) $\theta = 90°$ and $\varphi = 0°$, (b) $\theta = 90°$ and $\varphi = 90°$.
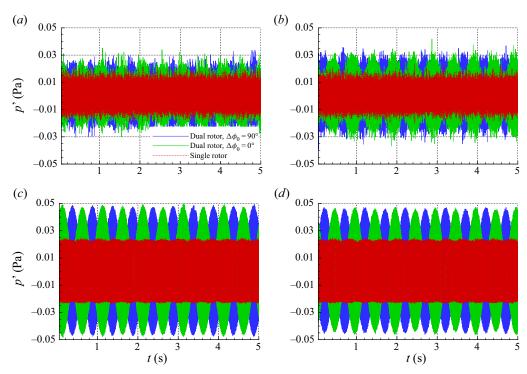

Figure 29. Computed time signals at different observers of two rotors with slight difference in RPS_0 of 99.5 and 100.5. The actual RPS is perturbed with periodic (with $f_n = 1000\,\text{Hz}$ and $A_n = 10^{-3}$) and random (with $f_c = 500\,\text{Hz}$ and $A_G = 0.5 \times 10^{-8}$) fluctuations; (a) $\theta = 30°$ and $\varphi = 0°$, (b) $\theta = 30°$ and $\varphi = 90°$, (c) $\theta = 90°$ and $\varphi = 0°$, (d) $\theta = 90°$ and $\varphi = 90°$.

There are discernible differences at higher frequencies, but the levels are much lower. By contrast, significant differences are found at $\varphi = 90°$. Particularly, the tonal noise at the BPF is not seen for counter-rotating rotors, which is likely cancelled due to interference. In this work, we also compute the OASPL (from 50 to 5000 Hz) at different observer angles to better visualise the directivity. As shown in figure 31, the noise levels have
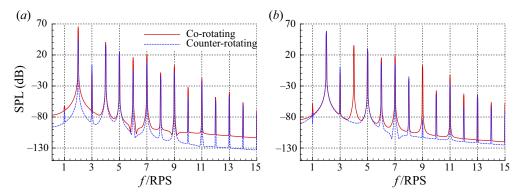
956 A16-26

Figure 30. Computed noise spectra for dual rotors with different configurations. Both rotors have the same averaged rotation speed $RPS_0 = 100$. Here, $\Delta\phi_0 = 45°$ and there are periodic fluctuations in RPS ($f_n = 500$ Hz and $A_n = 10^{-3}$); (a) $\theta = 90°$ and $\varphi = 0°$, (b) $\theta = 90°$ and $\varphi = 90°$.
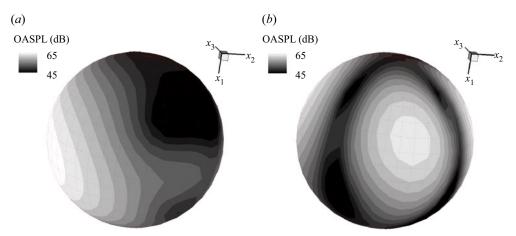

Figure 31. Computed directivity of dual rotors with different configurations. Both rotors have the same averaged rotation speed $RPS_0 = 100$. Here, $\Delta\phi_0 = 45°$ and there are periodic fluctuations in RPS ($f_n = 500$ Hz and $A_n = 10^{-3}$); (a) co-rotating, (b) counter-rotating.

distinguishable patterns for both configurations. Both rotation direction and initial phase angle difference can affect the noise directivity. However, if there are slight differences in the mean rotation speeds, e.g. $RPS_0 = 99.5$ and 100.5, respectively, the interference effect will be significantly altered. As shown in figure 32, the spectra by both co-rotating and counter-rotating configurations are close. Also, for the same polar observer angle $\theta = 90°$, the results at different azimuthal angles $\varphi = 0°$ and $90°$ are close. Figure 33 shows the directivity patterns of the OASPL computed from 50 to 5000 Hz. The noise radiation in different angles is axisymmetric, and the results for co-rotating and counter-rotating rotors are close.

5. Summary

This work studies the influence of rotation speed variation and deviation, blade vibration and geometry asymmetry on rotor noise using a time-domain theoretical formulation. The effects of irregular motions are explicitly included in the source coordinate to simplify the
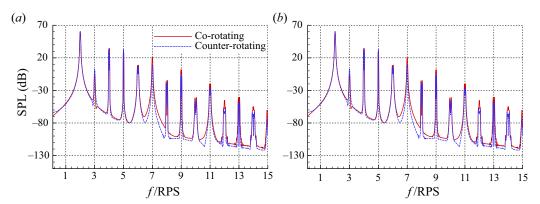
(*a*)

(*b*)

Figure 32. Computed noise spectra for different dual rotor configurations. There mean rotation speeds of the rotors are $RPS_0 = 99.5$ and 100.5, respectively. Here, $\Delta\phi_0 = 45°$ and there are periodic fluctuations in RPS ($f_n = 500$ Hz and $A_n = 10^{-3}$); (*a*) $\theta = 90°$ and $\varphi = 0°$, (*b*) $\theta = 90°$ and $\varphi = 90°$.
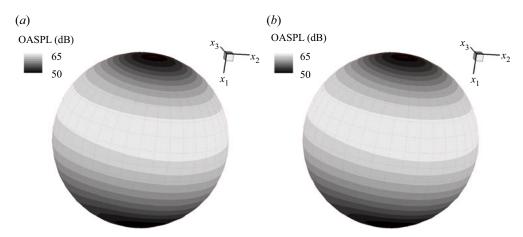
(*a*)

(*b*)

Figure 33. Computed directivity of dual rotors for different dual rotor configurations. The mean rotation speeds of the rotors are $RPS_0 = 99.5$ and 100.5, respectively. Here, $\Delta\phi_0 = 45°$ and there are periodic fluctuations in RPS ($f_n = 500$ Hz and $A_n = 10^{-3}$); (*a*) co-rotating, (*b*) counter-rotating.

computation and efficiently estimate the retarded time. The noise sources are modelled using aerodynamic variables from the BEMT method. The amplitudes of the factors under investigation are assumed to be small. The accuracy of the prediction model is validated by comparing it with experiments and high-fidelity CAA simulations. The rotation speed deviation due to the motor control accuracy can alter the BPF and SPLs. If periodic fluctuations are present, multiple tonal noise components at various frequencies dependent on both BPF and f_n will be produced. The increment is more significant when f_n is high. If the rotation speed fluctuation is random, broadband-type noise is produced, especially in the upstream and downstream directions. The blade vibration can produce dipole-like noise perpendicular to the rotation plane. The periodic vibration can cause multiple tones, while the random fluctuation can lead to broadband noise increase. The asymmetric geometry of the rotor blades, which can cause a mass imbalance in practice, will lead to tonal noise at multiple frequencies that results from combinations of the RPS and the original peaks in the spectra. The acoustic feature of the dual rotor system is

956 A16-28

also investigated. If the rotation speeds are identical, the initial phase angle difference $\Delta\phi_0$ and relative rotation directions can significantly affect the sound distribution due to the interference effect. However, if the uncertainty factor is such that slight deviations of the rotation speeds exist for both blades, wave packets are formed due to the rotation speed difference. The phase angle difference varies with time, making the resulting spectra insensitive to $\Delta\phi_0$.

Declaration of interests. The authors report no conflict of interest.

Author ORCIDs.

Siyang Zhong https://orcid.org/0000-0001-8235-0706;

Peng Zhou https://orcid.org/0000-0003-4936-9661;

Hanbo Jiang https://orcid.org/0000-0002-0228-919X;

Han Wu https://orcid.org/0000-0002-2797-8303.

Appendix A. Remarks on numerical implementation

At x, the computed sound pressure based on (2.12) is represented at the observer time t. The noise contributions by both Q and L_i are evaluated at the retarded time $\tau = t - R/a_\infty$, which, unfortunately, is challenging because $R = R(x(t), y(\tau))$ is implicitly dependent on the source τ. Moreover, when the rotation speed Ω varies with time, the source locations are computed as

$$y_2(\tau) = \eta \cos\left(\phi + \int_0^\tau \Omega(s)\,\mathrm{d}s\right), \quad y_3(\tau) = \eta \sin\left(\phi + \int_0^\tau \Omega(s)\,\mathrm{d}s\right), \quad (A1a,b)$$

making the nonlinear integral solution difficult to solve. Alternatively, in practical application, it is common that the observer location x is unchanged with the observing time t. In this case, it is easy to use the source-time-dominant algorithm to account for the retarded time effect (Brentner & Farassat 2003). Nevertheless, the detailed procedures for the current formulation is presented for completeness.

For a given source time τ, the source coordinates $y(\tau)$ can be determined, and the delayed observing time t is explicitly computed as

$$t = \tau + \frac{R(x, y(\tau))}{a_\infty}. \quad (A2)$$

However, for different source points emitting sound at time τ, the resulting observing times t at a given observer x are different. For convenience, the blade surface is discretised into N panels, and the centre of each panel is denoted as $y_n \in [y_1, y_2, \ldots, y_N]$. Both the source location and source strength are evaluated at different time steps of $\tau^m \in [\tau^1, \tau^2, \ldots, \tau^M]$. The two integral kernels in (2.12) are denoted as Θ and Π. The values at the source location y_n and time τ^m can be evaluated as Θ_n^m and Π_n^m, respectively. In addition, the corresponding observing time t_n^m is evaluated by using (A2). Therefore, when m ranges from $m = 1$ to M, we have an array of observing time $T_n = [t_n^1, t_n^2, \ldots, t_n^M]$ and the

956 A16-29

corresponding arrays of Θ and Π as

$$\left.\begin{aligned}\boldsymbol{\Theta}_n(\boldsymbol{T}_n) &= [\Theta_n^1(t_n^1), \Theta_n^2(t_n^2), \ldots, \Theta_n^M(t_n^M)],\\ \boldsymbol{\Pi}_n(\boldsymbol{T}_n) &= [\Pi_n^1(t_n^1), \Pi_n^2(t_n^2), \ldots, \Pi_n^M(t_n^M)].\end{aligned}\right\} \quad (A3)$$

Therefore, to ensure noise contribution by all discretised panels can be accounted for, we define a constant observing time array $\boldsymbol{T} = [t^1, t^2, \ldots, t^{\mathcal{M}}]$ with a constant interval of Δt. Therefore, the values of $\boldsymbol{\Theta}_n(\boldsymbol{T}_n)$ and $\boldsymbol{\Pi}_n(\boldsymbol{T}_n)$ in (A3) are employed to evaluate the values at the time steps in $\boldsymbol{T}$ (i.e. by using interpolation) as

$$\left.\begin{aligned}\overline{\boldsymbol{\Theta}_n}(\boldsymbol{T}) &= [\overline{\Theta_n^1}(t^1), \overline{\Theta_n^2}(t^2), \ldots, \overline{\Theta_n^{\mathcal{M}}}(t^{\mathcal{M}})],\\ \overline{\boldsymbol{\Pi}_n}(\boldsymbol{T}) &= [\overline{\Pi_n^1}(t^1), \overline{\Pi_n^2}(t^2), \ldots, \overline{\Pi_n^{\mathcal{M}}}(t^{\mathcal{M}})].\end{aligned}\right\} \quad (A4)$$

Then, an array of sound pressure at $\boldsymbol{T} = [t^1, t^2, \ldots, t^{\mathcal{M}}]$ can be computed as

$$\boldsymbol{P}(\boldsymbol{x}, \boldsymbol{T}) = [p'(\boldsymbol{x}, t^1), p'(\boldsymbol{x}, t^2), \ldots, p'(\boldsymbol{x}, t^{\mathcal{M}})] = \frac{\partial}{\partial t}\left(\sum_{n=1}^N \overline{\boldsymbol{\Theta}_n}(\boldsymbol{T})\right) - \sum_{n=1}^N \overline{\boldsymbol{\Pi}_n}(\boldsymbol{T}), \quad (A5)$$

and the temporal derivative can be easily evaluated by using a finite difference method using the temporal arrays.

REFERENCES

AL HADDAD, C., CHANIOTAKIS, E., STRAUBINGER, A., PLÖTNER, K. & ANTONIOU, C. 2020 Factors affecting the adoption and use of urban air mobility. *Transp. Res.* A **132**, 696–712.

ALTINORS, A., YOL, F. & YAMAN, O. 2021 A sound based method for fault detection with statistical feature extraction in UAV motors. *Appl. Acoust.* **183**, 108325.

ALVAREZ, E. & NING, A. 2020 High-fidelity modeling of multirotor aerodynamic interactions for aircraft design. *AIAA J.* **58** (10), 4385–4400.

ARNOLDI, R.A. 1956 Propeller noise caused by blade thickness. *Rep.* R-0896-1. United Aircraft Corporation.

BERNARDINI, G., CENTRACCHIO, F., GENNARETTI, M., IEMMA, U., PASQUALI, C., POGGI, C., ROSSETTI, M. & SERAFINI, J. 2020 Numerical characterisation of the aeroacoustic signature of propeller arrays for distributed electric propulsion. *Appl. Sci.* **10** (8), 2643.

BERNARDINI, G., GENNARETTI, M. & TESTA, C. 2016 Spectral-boundary-integral compact-source formulation for aero-hydroacoustics of rotors. *AIAA J.* **54** (11), 3349–3360.

BEST, S. 1945 Propeller balancing problems. *SAE Trans.* **53**, 648–659.

BIOT, M. 1940 Coupled oscillations of aircraft engine-propeller systems. *J. Aero. Sci.* **7** (9), 376–382.

BLOKHINTZEV, D. 1946 The propagation of sound in an inhomogeneous and moving medium I. *J. Acoust. Soc. Am.* **18** (2), 322–328.

BONDYRA, A., GASIOR, P., GARDECKI, S. & KASIŃSKI, A. 2017 Fault diagnosis and condition monitoring of UAV rotor using signal processing. In *2017 Signal Processing: Algorithms, Architectures, Arrangements, and Applications (SPA)*, pp. 233–238. IEEE.

BRENTNER, K.S. & FARASSAT, F. 1998 Analytical comparison of the acoustic analogy and Kirchhoff formulation for moving surfaces. *AIAA J.* **36** (8), 1379–1386.

BRENTNER, K.S. & FARASSAT, F. 2003 Modeling aerodynamically generated sound of helicopter rotors. *Prog. Aeronaut. Sci.* **39** (2-3), 83–120.

BU, H., MA, Z. & ZHONG, S. 2022 An experimental investigation of noise characteristics of overlapping propellers. *J. Acoust. Soc. Am.* **152** (1), 591–600.

BU, H., WU, H., BERTIN, C., FANG, Y. & ZHONG, S. 2021 Aerodynamic and acoustic measurements of dual small-scale propellers. *J. Sound Vib.* **511**, 116330.

CASALINO, D. 2003 An advanced time approach for acoustic analogy predictions. *J. Sound Vib.* **261** (4), 583–612.

CLEVELAND, W.S. 1979 Robust locally weighted regression and smoothing scatterplots. *J. Am. Stat. Assoc.* **74** (368), 829–836.

CURLE, N. 1955 The influence of solid boundaries upon aerodynamic sound. *Proc. R. Soc. Lond.* A **231** (1187), 505–514.

DARLOW, M. 2012 *Balancing of High-Speed Machinery*. Springer Science & Business Media.

DAVOUDI, B., TAHERI, E., DURAISAMY, K., JAYARAMAN, B. & KOLMANOVSKY, I. 2020 Quad-rotor flight simulation in realistic atmospheric conditions. *AIAA J.* **58** (5), 1992–2004.

DEMING, A.F. 1937 Noise from propellers with symmetrical sections at zero blade angle. *NACA Tech. Note* 605.

DEMING, A.F. 1940 Propeller rotation noise due to torque and thrust. *J. Acoust. Soc. Am.* **12** (1), 173–182.

DJUREK, I., PETOSIC, A., GRUBESA, S. & SUHANEK, M. 2020 Analysis of a quadcopter's acoustic signature in different flight regimes. *IEEE Access* **8**, 10662–10670.

DONATEO, T., DE PASCALIS, C.L., STRAFELLA, L. & FICARELLA, A. 2021 Off-line and on-line optimization of the energy management strategy in a hybrid electric helicopter for urban air-mobility. *Aero. Sci. Technol.* **113**, 106677.

FARASSAT, F. 1981 Linear acoustic formulas for calculation of rotating blade noise. *AIAA J.* **19** (9), 1122–1130.

FARASSAT, F. 1986 Prediction of advanced propeller noise in the time domain. *AIAA J.* **24** (4), 578–584.

FARASSAT, F. & BRENTNER, K.S. 1988 The uses and abuses of the acoustic analogy in helicopter rotor noise prediction. *J. Am. Helicopter Soc.* **33** (1), 29–36.

FARASSAT, F., DUNN, M.H. & SPENCE, P.L. 1992 Advanced propeller noise prediction in the time domain. *AIAA J.* **30** (9), 2337–2340.

FARASSAT, F. & SUCCI, G.P. 1980 A review of propeller discrete frequency noise prediction technology with emphasis on two current methods for time domain calculations. *J. Sound Vib.* **71** (3), 399–419.

FATTAH, R., CHEN, W.J., WU, H., WU, Y. & ZHANG, X. 2019 Noise measurements of generic small-scale propellers. *AIAA Paper* 2019-2498.

FFOWCS WILLIAMS, J.E. & HAWKINGS, D.L. 1969 Sound generation by turbulence and surfaces in arbitrary motion. *Proc. R. Soc. Lond.* A **264** (1151), 321–342.

FLOREANO, D. & WOOD, R.J. 2015 Science, technology and the future of small autonomous drones. *Nature* **521** (7553), 460–466.

GARRICK, I.E. & WATKINS, C.E. 1953 A theoretical study of the effect of forward speed on the free-space sound-pressure field around propellers. *NACA Tech. Note* 3018.

GENNARETTI, M., BERNARDINI, G., SERAFINI, J., TRAINELLI, L., ROLANDO, A., SCANDROGLIO, A., RIVIELLO, L. & PAOLONE, E. 2015 Acoustic prediction of helicopter unsteady manoeuvres. In *Proc. 41st European Rotorcraft Forum (ERF 2015)*. Deutsche Gesellschaft Für Luft- und Raumfahrt.

GENNARETTI, M., TESTA, C. & BERNARDINI, G. 2013 An unsteady aerodynamic formulation for efficient rotor tonal noise prediction. *J. Sound Vib.* **332** (25), 6743–6754.

GEORGE, A.R. & CHOU, S.-T. 1986 A comparative study of tail rotor noise mechanisms. *J. Am. Helicopter Soc.* **31** (4), 36–42.

GHALAMCHI, B., JIA, Z. & MUELLER, M. 2019 Real-time vibration-based propeller fault diagnosis for multicopters. *IEEE/ASME Trans. Mechatron.* **25** (1), 395–405.

GHORBANIASL, G., SIOZOS-ROUSOULIS, L. & LACOR, C. 2016 A time-domain Kirchhoff formula for the convective acoustic wave equation. *Proc. R. Soc. Lond.* A **472** (2187), 20150689.

GOLDSTEIN, G.E. 1974 Unified approach to aerodynamic sound generation in the presence of solid boundaries. *J. Acoust. Soc. Am.* **56** (2), 497–509.

GUTIN, L. 1948 On the sound field of a rotating propeller. *NACA Tech. Memo.* 1195.

HANSON, D.B. & PARZYCH, D.J. 1993 Theory for noise of propellers in angular inflow with parametric studies and experimental verification. *NASA Contractor Rep.* 4499.

HU, F., HUSSAINI, M. & MANTHEY, J. 1996 Low-dissipation and low-dispersion Runge–Kutta schemes for computational acoustics. *J. Comput. Phys.* **124** (1), 177–191.

HUBBARD, H. 1953 Propeller-noise charts for transport airplanes. *NACA Tech. Note* 2968.

HUBBARD, H., LANSING, D. & RUNYAN, H. 1971 A review of rotating blade noise technology. *J. Sound Vib.* **19** (3), 227–249.

HUO, X., WANG, B., CHEN, S. & CHEN, W. 2020 Sensorless unbalance diagnosis of affiliated rotating chamber based on driving current of permanent magnet synchronous motor. *IEEE/ASME Trans. Mechatron.* **26** (6), 2899–2909.

IANNACE, G., CIABURRO, G. & TREMATERRA, A. 2019 Fault diagnosis for UAV blades using artificial neural network. *Robotics* **8** (3), 59.

IKEDA, T., ENOMOTO, S., YAMAMOTO, K. & AMEMIYA, K. 2013 On the modification of the ffowcs williams-hawkings integration for jet noise prediction. *AIAA Paper* 2013-2277.

ISLAM, R., HUSAIN, I., FARDOUN, A. & MCLAUGHLIN, K. 2007 Permanent magnet synchronous motor magnet designs with skewing for torque ripple and cogging torque reduction. In *2007 IEEE Industry Applications Annual Meeting*, pp. 1552–1559. IEEE.

DE JESUS RANGEL-MAGDALENO, J., UREÑA-UREÑA, J., HERNÁNDEZ, A. & PEREZ-RUBIO, C. 2018 Detection of unbalanced blade on UAV by means of audio signal. In *2018 IEEE International Autumn Meeting on Power, Electronics and Computing (ROPEC)*, pp. 1–5. IEEE.

JIANG, H., WU, H., CHEN, W., ZHOU, P., ZHONG, S., ZHANG, X., ZHOU, G. & CHEN, B. 2022 Toward high-efficiency low-noise propellers: a numerical and experimental study. *Phys. Fluids* **34** (7), 076116.

JIANG, H. & ZHANG, X. 2022 An acoustic-wave preserved artificial compressibility method for low-Mach-number aeroacoustic simulations. *J. Sound Vib.* **516**, 116505.

KIM, D., KO, J., SARAVANAN, V. & LEE, S. 2021 Stochastic analysis of a single-rotor to quantify the effect of RPS variation on noise of hovering multirotors. *Appl. Acoust.* **182**, 108224.

KIM, D.H., PARK, C.H. & MOON, Y.J. 2019 Aerodynamic analyses on the steady and unsteady loading-noise sources of drone propellers. *Intl J. Aeronaut. Space Sci.* **20** (3), 611–619.

KUANTAMA, E., MOLDOVAN, O., ȚARCĂ, I., VESSELÉNYI, T. & ȚARCĂ, R. 2021 Analysis of quadcopter propeller vibration based on laser vibrometer. *J. Low Freq. Noise Vib. Active Control* **40** (1), 239–251.

KURTZ, D. & MARTE, J. 1970 A review of aerodynamic noise from propellers, rotors, and lift fans. *NASA Tech. Rep.* 32-1462.

LEE, H. & LEE, D. 2020 Rotor interactional effects on aerodynamic and noise characteristics of a small multirotor unmanned aerial vehicle. *Phys. Fluids* **32** (4), 047107.

LEISHMAN, G. 2006 *Principles of Helicopter Aerodynamics*, 2nd edn. Cambridge University Press.

LIGHTHILL, M.J. 1952 On sound generated aerodynamically. I. General theory. *Proc. R. Soc. Lond.* A **211** (1107), 564–587.

LOPES, L.V. 2017 Compact assumption applied to monopole term of Farassat's formulations. *J. Aircraft* **54** (5), 1649–1663.

LOWSON, M.V. 1965 The sound field for singularities in motion. *Proc. R. Soc. Lond.* A **286** (1407), 559–572.

LOWSON, M.V. & OLLERHEAD, J.B. 1969 A theoretical study of helicopter rotor noise. *J. Sound Vib.* **9** (2), 197–222.

MANI, R. 1990 The radiation of sound from a propeller at angle of attack. *Proc. R. Soc. Lond.* A **431** (1882), 203–218.

MARQUÉS, P. & DA RONCH, A. 2017 *Advanced UAV Aerodynamics, Flight Stability and Control: Novel Concepts, Theory and Applications*. John Wiley & Sons.

MCKAY, R. & KINGAN, M.J. 2019 Multirotor unmanned aerial system propeller noise caused by unsteady blade motion. *AIAA Paper* 2019-2499.

NAJAFI-YAZDI, A., BRÈS, G. & MONGEAU, L. 2011 An acoustic analogy formulation for moving sources in uniformly moving media. *Proc. R. Soc. Lond.* A **467** (2125), 144–165.

NIEMIEC, R. & GANDHI, F. 2017 Effect of elastic blade deformation on trim and vibratory loads of a quadcopter. In *Proceedings of the 73rd American Helicopter Society Annual Forum, Fort Worth, Texas*, pp. 2017–2073. American Helicopter Society International.

NIEMIEC, R., GANDHI, F. & KOPYT, N. 2022 Relative rotor phasing for multicopter vibratory load minimisation. *Aeronaut. J.* **126** (1298), 710–729.

NING, Z., WLEZIEN, R.W. & HU, H. 2017 An experimental study on small UAV propellers with serrated trailing edges. *AIAA Paper* 2017-3813.

NOWICKI, N. 2017 Measurement and modeling of multicopter UAS rotor blade deflections in hover. *NASA Contractor Rep.* CR-2017-219428.

PREISSER, J., BROOKS, T. & MARTIN, R. 1994 Recent studies of rotorcraft blade-vortex interaction noise. *J. Aircraft* **31** (5), 1009–1015.

RAJENDRAN, S. & SRINIVAS, S. 2020 Air taxi service for urban mobility: a critical review of recent developments, future challenges, and opportunities. *Transp. Res.* E **143**, 102090.

SEMKE, W., ZAHUI, D. & SCHWALB, J. 2021 The vibration and acoustic effects of prop design and unbalance on small unmanned aircraft. In *Sensors and Instrumentation, Aircraft/Aerospace, Energy Harvesting & Dynamic Environments Testing*, vol. 7, pp. 9–16. Springer.

SHUKLA, D. & KOMERATH, N. 2018 Multirotor drone aerodynamic interaction investigation. *Drones* **2** (4), 43.

SHUR, M.L., SPALART, P.R. & STRELETS, M.K. 2005 Noise prediction for increasingly complex jets. Part I: methods and tests. *Intl J. Aeroacoust.* **4** (3–4), 213–246.

SINIBALDI, G. & MARINO, L. 2013 Experimental analysis on the noise of propellers for small UAV. *Appl. Acoust.* **74** (1), 79–88.

SPLETTSTOESSER, W.R., KUBE, R., WAGNER, W., SEELHORST, U., BOUTIER, A., MICHELI, F., MERCKER, E. & PENGEL, K. 1997 Key results from a higher harmonic control aeroacoustic rotor test (HART). *J. Am. Helicopter Soc.* **42** (1), 58–78.

STEPHENSON, J.H., WEITSMAN, D. & ZAWODNY, N.S. 2019 Effects of flow recirculation on unmanned aircraft system (UAS) acoustic measurements in closed anechoic chambers. *J. Acoust. Soc. Am.* **145** (3), 1153–1155.

TIAN, J., ZHANG, Z., NI, Z. & HUA, H. 2017 Flow-induced vibration analysis of elastic propellers in a cyclic inflow: an experimental and numerical study. *Appl. Ocean Res.* **65**, 47–59.

TINNEY, C.E. & SIROHI, J. 2018 Multirotor drone noise at static thrust. *AIAA J.* **56** (7), 2816–2826.

VAN DER WALL, B.G. & LEISHMAN, J.G. 1994 On the influence of time-varying flow velocity on unsteady aerodynamics. *J. Am. Helicopter Soc.* **39** (4), 25–36.

DE VRIES, R., VAN ARNHEM, N., SINNIGE, T., VOS, R. & VELDHUIS, L.L. 2021 Aerodynamic interaction between propellers of a distributed-propulsion system in forward flight. *Aero. Sci. Technol.* **118**, 107009.

WATKINS, S., BURRY, J., MOHAMED, A., MARINO, M., PRUDDEN, S., FISHER, A., KLOET, N., JAKOBI, T. & CLOTHIER, R. 2020 Ten questions concerning the use of drones in urban environments. *Build. Environ.* **167**, 106458.

WRIGHT, S.E. 1971 Discrete radiation from rotating periodic sources. *J. Sound Vib.* **17** (4), 437–498.

WRIGHT, M. & MORFEY, C.L. 2015 On the extrapolation of acoustic waves from flow simulations with vortical out flow. *Intl J. Aeroacoust.* **14** (1–2), 217–227.

WU, H., CHEN, W., FATTAH, R., FANG, Y., ZHONG, S. & ZHANG, X. 2020 A rotor blade aeroacoustics test platform at HKUST. In *INTER-NOISE and NOISE-CON Congress and Conference Proceedings*, vol. 261, pp. 2476–2484. Institute of Noise Control Engineering.

WU, H., JIANG, H., ZHOU, P., ZHONG, S., ZHANG, X., ZHOU, G. & CHEN, B. 2022 On identifying the deterministic components of propeller noise. *Aero. Sci. Technol.* **130**, 107948.

XU, D., SUN, Y., NG, D. & SCHOBER, R. 2020 Multiuser MISO UAV communications in uncertain environments with no-fly zones: robust trajectory and resource allocation design. *IEEE Trans. Commun.* **68** (5), 3153–3172.

YAO, P., WANG, H. & SU, Z. 2016 Cooperative path planning with applications to target tracking and obstacle avoidance for multi-UAVs. *Aero. Sci. Technol.* **54**, 10–22.

YI, W., ZHOU, P., FANG, Y., GUO, J., ZHONG, S., ZHANG, X., HUANG, X., ZHOU, G. & CHEN, B. 2021 Design and characterization of a multifunctional low-speed anechoic wind tunnel at HKUST. *Aero. Sci. Technol.* **115**, 106814.

YUNG, H. 2000 Rotor blade–vortex interaction noise. *Prog. Aerosp. Sci.* **36** (2), 97–115.

ZAWODNY, N.S., BOYD, D.D. JR. & BURLEY, C.L. 2016 Acoustic characterization and prediction of representative, small-scale rotary-wing unmanned aircraft system components. *NASA Tech. Rep.* NF1676L-22587.

ZHONG, S. & ZHANG, X. 2017 A sound extrapolation method for aeroacoustics far-field prediction in presence of vortical waves. *J. Fluid Mech.* **820**, 424–450.

ZHONG, S. & ZHANG, X. 2018 A generalized sound extrapolation method for turbulent flows. *Proc. R. Soc. Lond.* A **474** (2210), 20170614.

ZHONG, S., ZHOU, P., FATTAH, R. & ZHANG, X. 2020 A revisit of the tonal noise of small rotors. *Proc. R. Soc. Lond.* A **476** (2244), 20200491.

ZHOU, T. & FATTAH, R. 2017 Tonal noise characteristics of two small-scale propellers. *AIAA Paper* 2017-4054.

ZHOU, W., NING, Z., LI, H. & HU, H. 2017 An experimental investigation on rotor-to-rotor interactions of small UAV propellers. *AIAA Paper* 2017-3744.